Article

Ligand-engineered bandgap stability in mixed-halide perovskite LEDs

https://doi.org/10.1038/s41586-021-03217-8

Received: 3 July 2020

Accepted: 11 January 2021

Published online: 3 March 2021

Check for updates

Yasser Hassan[1,15]✉, Jong Hyun Park[2,15], Michael L. Crawford[3], Aditya Sadhanala[1,4,5], Jeongjae Lee[6], James C. Sadighian[3], Edoardo Mosconi[7], Ravichandran Shivanna[5], Eros Radicchi[7,8], Mingyu Jeong[9], Changduk Yang[9], Hyosung Choi[10], Sung Heum Park[11], Myoung Hoon Song[2], Filippo De Angelis[7,8,12], Cathy Y. Wong[3,13,14]✉, Richard H. Friend[5], Bo Ram Lee[11]✉ & Henry J. Snaith[1]✉

Lead halide perovskites are promising semiconductors for light-emitting applications because they exhibit bright, bandgap-tunable luminescence with high colour purity[1,2]. Photoluminescence quantum yields close to unity have been achieved for perovskite nanocrystals across a broad range of emission colours, and light-emitting diodes with external quantum efficiencies exceeding 20 per cent—approaching those of commercial organic light-emitting diodes—have been demonstrated in both the infrared and the green emission channels[1,3,4]. However, owing to the formation of lower-bandgap iodide-rich domains, efficient and colour-stable red electroluminescence from mixed-halide perovskites has not yet been realized[5,6]. Here we report the treatment of mixed-halide perovskite nanocrystals with multidentate ligands to suppress halide segregation under electroluminescent operation. We demonstrate colour-stable, red emission centred at 620 nanometres, with an electroluminescence external quantum efficiency of 20.3 per cent. We show that a key function of the ligand treatment is to 'clean' the nanocrystal surface through the removal of lead atoms. Density functional theory calculations reveal that the binding between the ligands and the nanocrystal surface suppresses the formation of iodine Frenkel defects, which in turn inhibits halide segregation. Our work exemplifies how the functionality of metal halide perovskites is extremely sensitive to the nature of the (nano)crystalline surface and presents a route through which to control the formation and migration of surface defects. This is critical to achieve bandgap stability for light emission and could also have a broader impact on other optoelectronic applications—such as photovoltaics—for which bandgap stability is required.

The bandgap of metal halide perovskites can be tuned by several means, such as quantum confinement[7–10] in nanocrystals[5,6] and in two-dimensional perovskites[11–14], or by varying the halide composition in the ABX_3 perovskite stoichiometry, where A is an organic ammonium or alkali metal cation, B is a group 14 metal cation (typically lead) and X_3 are halide anions[5,6,15–17]. Using a mixture of iodide and bromide ions, nanocrystals with red emission between 615 nm and 640 nm—as required for displays—can be obtained with a photoluminescence quantum yield (PLQY) approaching unity[5,6,15,16]. However, these nanocrystals are susceptible to halide segregation on photoexcitation and on the application of electrical bias[5,18–20]. Despite much effort, colour-stable red electroluminescence from mixed-halide perovskite nanocrystals has not yet been realized[5,11–15,17,21–28].

Recent investigations have suggested that halide segregation occurs through the diffusion of vacancy and interstitial defects[18,19]. In mixed-halide perovskite films measured experimentally and in pure iodide systems studied computationally, halide defects seem to migrate to grain boundaries or to crystal surfaces[29–34]. For polycrystalline films, improvements in bandgap stability and device efficiency have been achieved by passivating grain boundaries with alkali-metal halides or with larger organic ammonium cations[7,8,11,17,27,35]. For nanocrystals, interfacial passivation is of particular

[1]Clarendon Laboratory, Department of Physics, University of Oxford, Oxford, UK. [2]Department of Materials Science and Engineering, Ulsan National Institute of Science and Technology (UNIST), Ulsan, Republic of Korea. [3]Department of Chemistry and Biochemistry, University of Oregon, Eugene, OR, USA. [4]Centre for Nano Science and Engineering, Indian Institute of Science, Bangalore, India. [5]Cavendish Laboratory, University of Cambridge, Cambridge, UK. [6]School of Earth and Environmental Sciences, Seoul National University, Seoul, Republic of Korea. [7]Computational Laboratory for Hybrid/Organic Photovoltaics (CLHYO), Istituto CNR di Scienze e Tecnologie Chimiche 'Giulio Natta' (CNR-SCITEC), Perugia, Italy. [8]Department of Chemistry, Biology and Biotechnology, University of Perugia, Perugia, Italy. [9]Department of Energy Engineering, School of Energy and Chemical Engineering, Perovtronics Research Center, Low Dimensional Carbon Materials Center, Ulsan National Institute of Science and Technology (UNIST), Ulsan, Republic of Korea. [10]Department of Chemistry, Research Institute for Convergence of Basic Sciences, Research Institute for Natural Sciences, Hanyang University, Seoul, Republic of Korea. [11]Department of Physics, Pukyong National University, Busan, Republic of Korea. [12]CompuNet, Istituto Italiano di Tecnologia, Genoa, Italy. [13]Materials Science Institute, University of Oregon, Eugene, OR, USA. [14]Oregon Center for Optical, Molecular, and Quantum Science, University of Oregon, Eugene, OR, USA. [15]These authors contributed equally: Yasser Hassan, Jong Hyun Park. ✉e-mail: yasserhassan8085@gmail.com; cwong3@uoregon.edu; brlee@pknu.ac.kr; henry.snaith@physics.ox.ac.uk

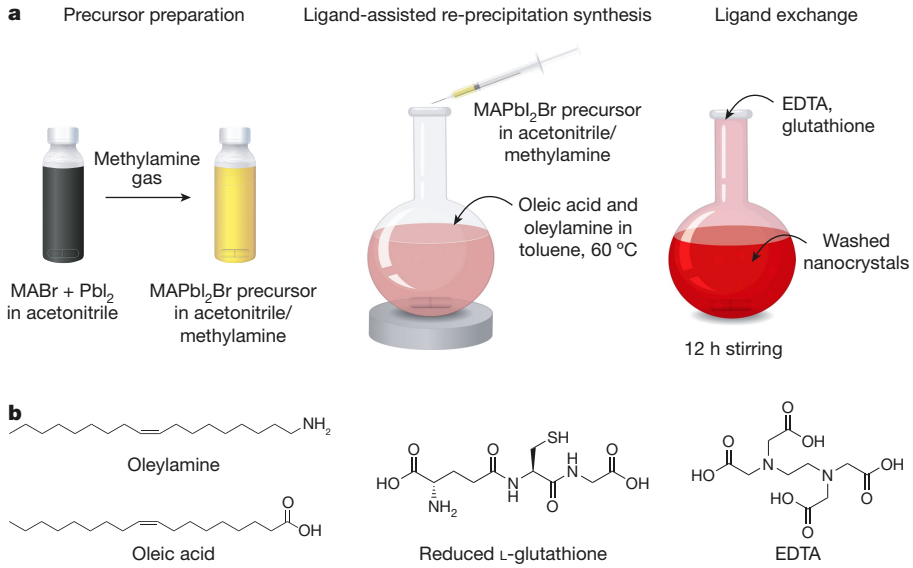

Fig. 1 | Nanocrystal synthesis. a, Synthesis and ligand treatment steps: the dissolution of perovskite precursors in acetonitrile and methylamine; nanocrystal synthesis using a modified ligand-assisted re-precipitation method; and post-synthetic ligand treatment. **b**, Chemical structures of the ligands used.

importance because of the high surface-area-to-volume ratio of nanocrystals and reports that halide segregation can occur both within (intra) and between (inter) nanocrystals[20,36]. One approach to resolving the issue of halide segregation in nanocrystals could involve a surface treatment that removes or immobilizes surface defects[5,15].

Here we synthesized $MAPb(I_xBr_{1-x})_3$ nanocrystals (where MA is methylammonium) using a modified ligand-assisted re-precipitation method[5]. After purification, we treated the nanocrystals with the ligands ethylenediaminetetraacetic acid (EDTA) and reduced L-glutathione (Fig. 1). These molecules bind strongly to lead in biological systems[37–40]. To assess the effect of the ligand treatment, we analysed time-resolved photoluminescence spectroscopy, PLQY, attenuated total reflection Fourier transform infrared spectroscopy (ATR-FTIR), X-ray photoelectron spectroscopy (XPS) and X-ray diffraction (XRD) measurements (Fig. 2, Extended Data Fig. 1).

As-synthesized $MAPb(I_xBr_{1-x})_3$ nanocrystals in toluene exhibit photoluminescence centred at 642 nm (Fig. 2a). After treatment with glutathione, we observed an increase in intensity of the photoluminescence peak and a blueshift to 625 nm (Fig. 2b). With EDTA, an increase in photoluminescence intensity was accompanied by a slight blueshift to 635 nm. Using an equimolar mixture of EDTA and glutathione, hereafter denoted E+G, we observed emission at 630 nm and an increase in photoluminescence intensity, PLQY and decay lifetime (Fig. 2b, c,

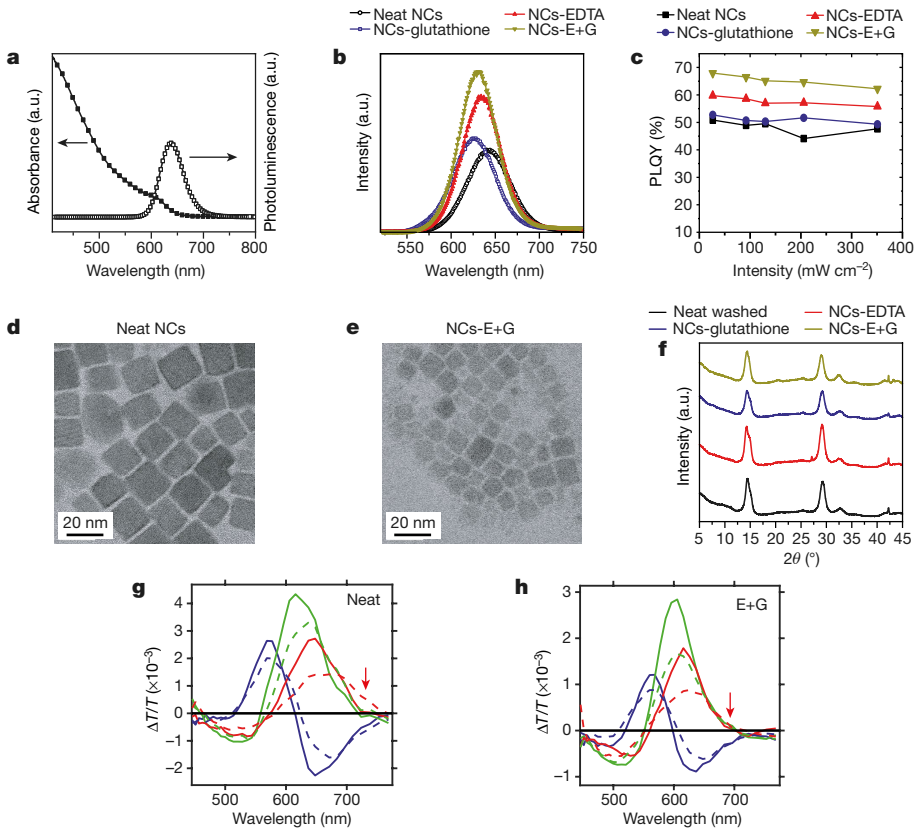

Fig. 2 | Effect of ligand treatment on the solution photoluminescence and the structural properties of the nanocrystals. a, Absorption and photoluminescence spectra of as-synthesized $MAPb(I_{1-x}Br_x)_3$ nanocrystals in solution. **b**, Photoluminescence spectra of nanocrystal films before and after post-synthetic treatment with glutathione, EDTA and E+G. **c**, Dependence of PLQY of the nanocrystal thin films on excitation fluence before and after ligand treatment, measured in an integrating sphere. **d**, **e**, HR-TEM images of neat nanocrystals (**d**) and nanocrystals after treatment with E+G (**e**). **f**, XRD spectra of the nanocrystal films before and after ligand treatment. **g**, **h**, DADS from a global fit of TAS measurements of neat (**g**) and E+G-capped (**h**) nanocrystals. Solid and dashed lines are spectra before and after 30 s exposure to a 7.1 W cm^{-2} 405 nm continuous-wave laser, respectively. Blue, green and red traces correspond to decay components with time constants of approximately 400 fs, 14 ps and 280 ps, respectively. Red arrows indicate the red edge of the spectra, where changes in the bandgap of the material would result in changes to the bleaching of the sample due to band filling. a.u., arbitrary units.

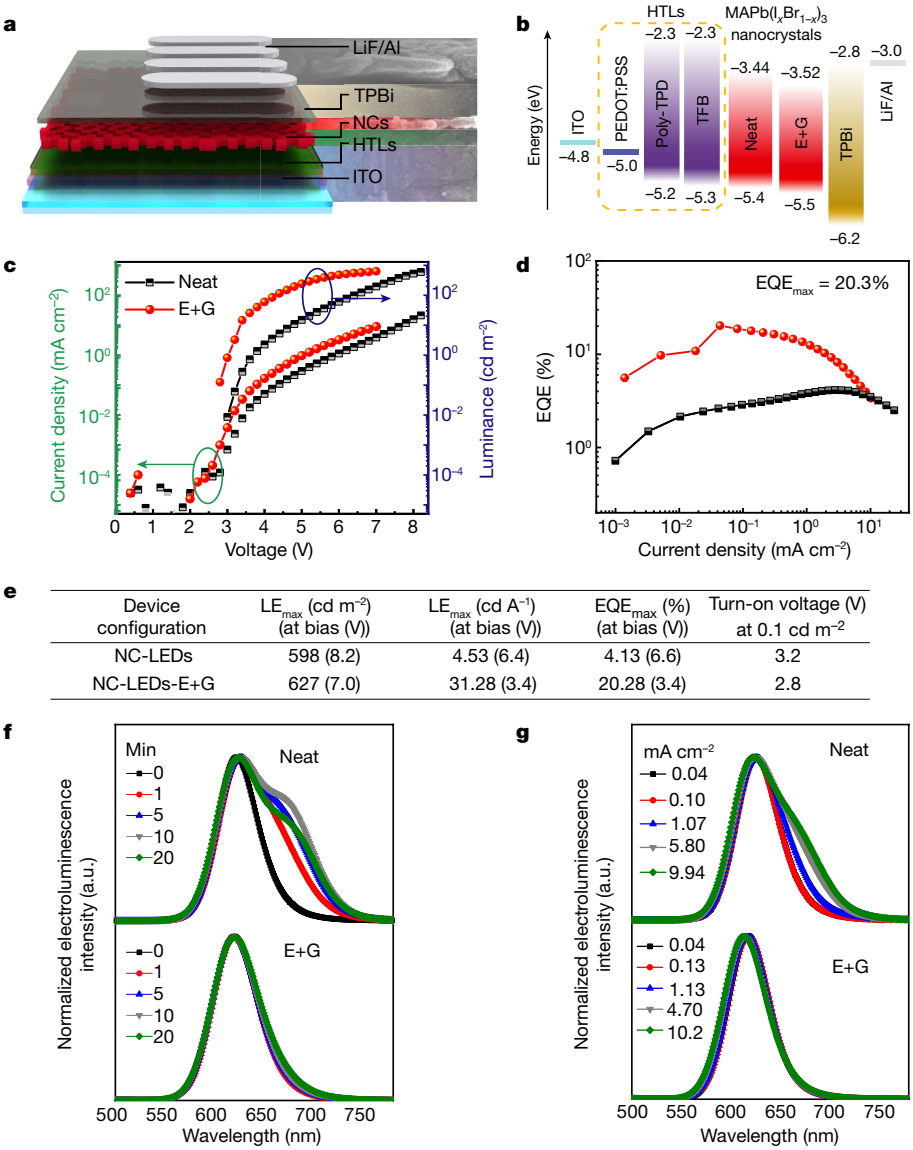

Device configuration	LE$_{max}$ (cd m^{-2}) (at bias (V))	LE$_{max}$ (cd A^{-1}) (at bias (V))	EQE$_{max}$ (%) (at bias (V))	Turn-on voltage (V) at 0.1 cd m^{-2}
NC-LEDs	598 (8.2)	4.53 (6.4)	4.13 (6.6)	3.2
NC-LEDs-E+G	627 (7.0)	31.28 (3.4)	20.28 (3.4)	2.8

Fig. 3 | Characterization of mixed-halide MAPb(I$_{1-x}$Br$_x$)$_3$ NC-LED devices. a, Schematic of the MAPb(I$_{1-x}$Br$_x$)$_3$ NC-LED architecture and an SEM image showing the cross-section of a device. The thicknesses of each layer, as confirmed by SEM, are as follows: PEDOT:PSS/poly-TPD/TFB hole-transporting layer (HTL) (30 nm), perovskite nanocrystal emission layer (20 nm), TPBi electron-transporting layer (70 nm), LiF/Al electrode (80 nm). ITO, indium tin oxide; PEDOT:PSS, poly(3,4-ethylenedioxythiophene): poly(*p*-styrene sulfonate; TBPi, 2,2′,2″-(1,3,5-benzinetriyl)-tris(1-phenyl-1*H*-benzimidazole; poly-TPD; poly(*N*,*N*′–bis(4-butylphenyl)-*N*,*N*′-bisphenylbenzidine); TFB, poly((9,9-dioctylfluorenyl-2,7-diyl)-co-(4,4′-(*N*-(4-s-butylphenyl)diphenylamine)). **b**, Energy band diagram of the materials used in these LEDs, showing bandgap values (in eV from vacuum) from refs. [47–49]. **c**–**e**, Operational characteristics for LEDs incorporating neat and E+G-treated nanocrystal layers. **c**, Current density–voltage (*J*–*V*) and luminance–voltage (*L*–*V*) curves; **d**, EQE–current density curves; **e**, device performance parameters of best-performing LEDs. LE, luminous efficiency. **f**, Electroluminescence spectra at different time intervals of LEDs held at a constant current density of 1.5 mA cm^{-2}. **g**, Electroluminescence spectra at different current densities (mA cm^{-2}).

Extended Data Fig. 1); this is consistent with ligand treatment resulting in a decrease in the total number of active defects. These data suggest that, of the ligand treatments we tested, E+G is the most favourable for suppressing non-radiative recombination. High-resolution transmission electron microscopy (HR-TEM) images show that E+G-treated nanocrystals are smaller than untreated, 'neat' nanocrystals (average cubic dimensions of 12 ± 1.7 nm and 16.3 ± 2 nm, respectively; Fig. 2d, e, Extended Data Fig. 2). For weakly confined excitons, the exciton energy is linearly dependent on the inverse square of the nanocrystal width. A blueshift in emission, consistent with quantum confinement and lattice relaxation, has been measured for perovskite nanoparticles within this size range[41]. Furthermore, we have previously observed a blueshift in emission of up to 80 nm due to quantum confinement effects in similarly sized $MAPbI_3$ nanocrystals[5]. We therefore expect the reduction in nanocrystal size as a result of ligand treatment to increase quantum confinement, contributing to the observed blueshift in emission[41].

Using XPS (Extended Data Fig. 1), we find that the I:Br ratio decreases from 2:1 in the precursor solution to approximately 2:3 in the synthesized nanocrystals. For this composition, we would expect a bulk emission at 647–655 nm. After ligand treatment, we observed a minor enrichment in bromide content, which would account for the up to 8 nm blueshift in emission of the E+G-treated sample[42]. On the basis of experiments in which the halide composition of polycrystalline MAPb(I$_{1-x}$Br$_x$)$_3$ films was varied[42], we would also expect a change in lattice constant of approximately 0.019 Å per 10 nm shift in the position of the photoluminescence peak; however, XRD measurements revealed a cubic lattice constant of 6.05 Å for the nanocrystal films both before and after ligand treatment (Fig. 2f). Collectively, these results suggest that both compositional changes and confinement effects influence the position of the emission peak.

To assess whether ligand treatment suppresses halide segregation and improves bandgap stability, we performed transient absorption spectroscopy (TAS) (Extended Data Fig. 3). We measured neat and E+G-treated nanocrystal films, as-prepared and after exposure to a 405-nm laser. A global fit of the signal yields decay-associated difference spectra (DADS) (Fig. 2g, h). The sub-ps decay measured using TAS arises from bandgap renormalization, Auger recombination and carrier cooling[43]. Carriers accumulate near the band edge, causing optical bleaching at these energies. The longest decay measured by TAS originates from carrier recombination. After irradiation for 30 s, spectra of the neat sample displayed a new low-energy bleach, which was visible in the longest DADS component. By contrast, the DADS line-shape for the E+G-treated sample remained approximately unchanged after irradiation. The emergence of the low-energy bleach in the neat sample is consistent with the emergence of lower-bandgap iodide-rich minority phases, from which charge carriers recombine; this is suppressed in the E+G treated sample.

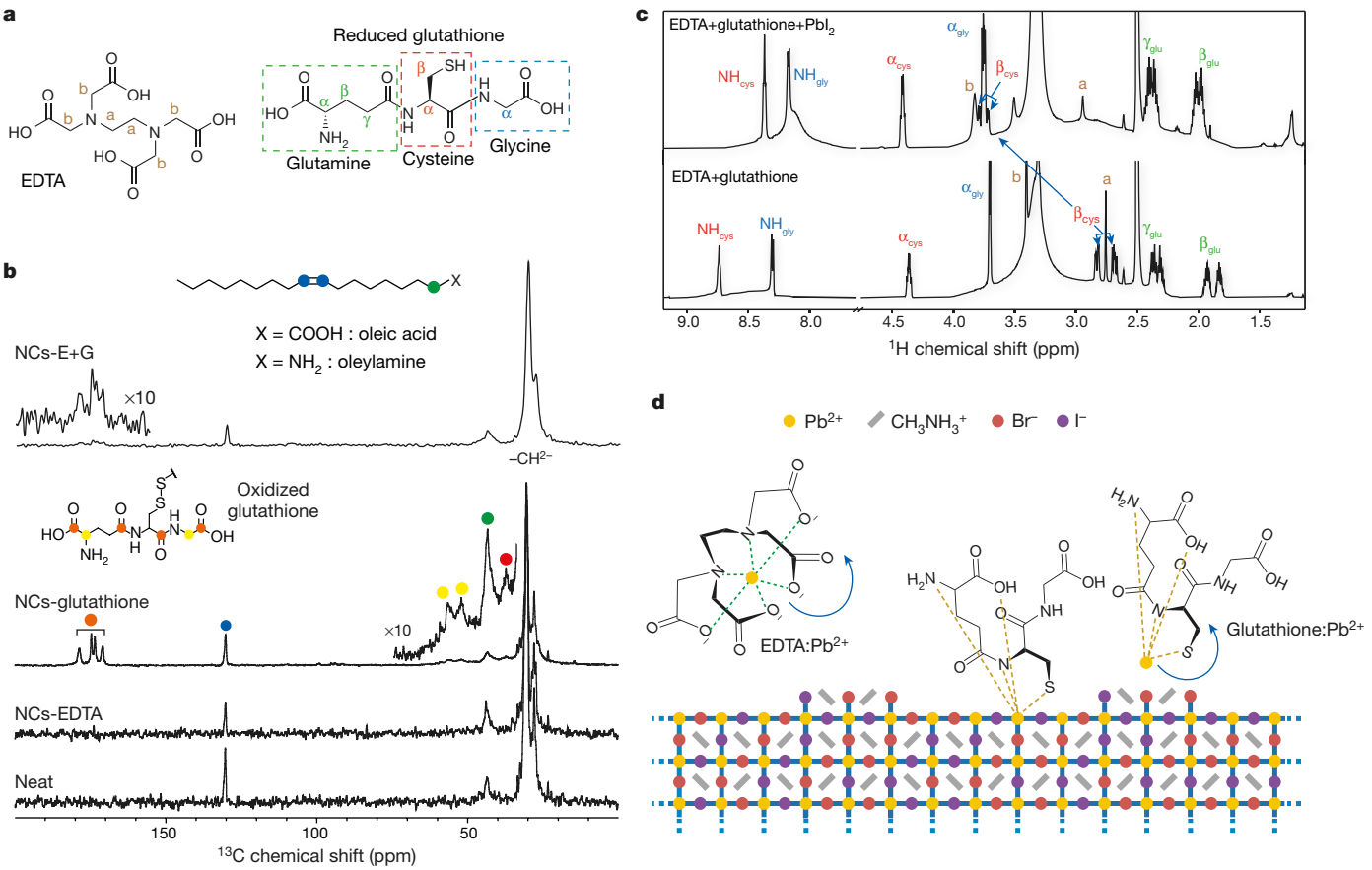

Fig. 4 | Characterization of interactions between the ligands and the nanocrystal surface using NMR spectroscopy. a, The structures of EDTA and glutathione. a and b label CH_2 groups of EDTA whereas α, β and γ label CH_2 groups in glutathione; see **c** for their corresponding NMR peaks. **b**, ^{13}C solid-state NMR spectra of neat and ligand (glutathione, EDTA, E+G)-treated nanocrystals. The insets show the structures of the ligands. **c**, Solution ^{1}H NMR spectra of E+G with and without PbI_2 in d_6-DMSO solution. **d**, The proposed molecular interactions of glutathione and EDTA with Pb^{2+} atoms on the nanocrystal surface.

Halide segregation between nanocrystals would result in the formation of Br-rich and I-rich nanocrystals. This has been observed in other perovskite nanocrystals and can result in a second, higher-energy photoluminescence emission in addition to the redshifted photoluminescence[20,36]. In Extended Data Fig. 4 we show that, even at very low nanocrystal concentrations in a polymer matrix, we observe redshifted emission with no growth of a high-energy peak nor broadening of the high-energy emission shoulder after irradiation. Confocal photoluminescence measurements on such films reveal a redshifted emission under illumination, which seems to arise from single nanocrystals. The lack of a high-energy feature in the transient absorption spectra of illuminated neat nanocrystals also indicates that Br-rich nanocrystals are not forming, suggesting that segregation can occur within individual nanocrystals.

We next assess the effect of ligand treatment on light-emitting diodes fabricated from these nanocrystals (NC-LEDs). We find that both EDTA and glutathione considerably suppress the halide segregation and improve bandgap stability, but EDTA-treated NC-LEDs exhibit a small broadening in the emission spectra during operation. Conversely, glutathione-treated NC-LEDs show the most stable emission spectra but a lower device efficiency. Efficient and colour-stable NC-LEDs were achieved with E+G treatment (Extended Data Fig. 5). To better understand the role of each ligand, we performed a second ligand-treatment step using the soft Lewis base 1-adamantanecarboxylic acid (ADAC). EDTA-, glutathione- and E+G-treated NC-LEDs show a negligible peak shift and small spectral broadening during operation. After subsequent treatment with ADAC, the EDTA- and E+G-treated nanocrystals exhibit more substantial peak shifting and broadening. By contrast, glutathione-treated NC-LEDs show stable electroluminescence, even after treatment with ADAC. These observations indicate that glutathione is more strongly bound to the nanocrystal surface than is EDTA; however, EDTA seems to be important for achieving the highest device efficiencies.

When choosing charge-injection layers and optimizing the performance of the LEDs, we found that maximizing the PLQY of half-constructed devices resulted in an effective selection of materials (Extended Data Figs. 6, 7). A schematic of our final device stack and a scanning electron microscopy (SEM) cross-sectional image are shown in Fig. 3a, b. We observed higher current densities in E+G-treated NC-LEDs compared to those treated with other ligands, and considerably improved external quantum efficiencies (EQEs) (Fig. 3c, d). We measured a maximum EQE of 20.3% at a current density of around 0.1 mA cm^{-2} and an emission wavelength of approximately 620 nm, placing these red perovskite LEDs in the same quantum efficiency range as commercial organic light-emitting diodes. Considering the PLQY of isolated perovskite nanocrystal films on glass, the refractive index of the perovskite layer, optical outcoupling and photon recycling, we estimate an internal PLQY of 0.88 (see Methods[44]). The effect of photon recycling and optical outcoupling in complete perovskite LEDs has previously been quantified, showing that EQEs of more than 20% are feasible for perovskite emission layers with high internal PLQY[45].

The most pressing challenge in the fabrication of red-emitting metal halide perovskites is achieving bandgap stability. In Fig. 3f, g we show the emission spectra of LEDs operating at a fixed current density over time and over a range of current densities, respectively. For the neat NC-LEDs held at a constant current density of 1.5 mA cm^{-2} measured

over 20 min, we observed a broadening of the emission peak and the emergence of a shoulder at around 680 nm. Similar results were obtained during measurements at current densities of 10 mA cm^{-2} (Extended Data Fig. 8). These observations are consistent with halide segregation driven by electrical biasing and/or current injection during LED operation and resulting in lower-energy emission from iodide-enriched regions. By contrast, the emission spectrum for the E+G-treated NC-LEDs is stable at 620 nm under the same operating conditions and duration. We note, however, that the absolute electroluminescence intensity decays over time. Extended Data Fig. 8 shows the luminance as a function of time for E+G-treated NC-LEDs held at current densities of 0.1, 1 and 10 mA^{-2}. The time taken for the luminance to decay to 50% of its initial value (T_{50}) decreased from 340 to 130 to 16 min, respectively, with increasing current density. These findings indicate that, although we have achieved colour-stable red emission, the challenge to deliver long-term stability in terms of absolute brightness and efficiency remains.

To understand the origin of the improvement in device performance when using ligand-treated nanocrystals, we needed to identify the key ligand–perovskite interactions that stabilize the nanocrystal surface. To this end, we performed solid-state ^{13}C nuclear magnetic resonance (NMR) studies on the nanocrystals both before and after treatment with E+G. The resulting data (Fig. 4a, b) show a clear peak at 130.2 ppm, which arises from the double-bonded carbons in the oleic acid and oleylamine molecules. This peak, alongside the aliphatic $-CH_2-$ peaks (30–27 ppm), clearly indicates the presence of oleic acid and oleylamine on the nanocrystal surface even after treatment with EDTA, glutathione or E+G; the nonpolar chains of these remaining oleic acid and oleylamine molecules probably ensure the solubility of the nanocrystals in toluene after the ligand treatment. The absence of EDTA peaks in the EDTA-treated sample shows that the amount of EDTA on the nanocrystal surface is below the NMR detection limit; however, clear peaks arising from the carbonyl and α-carbonyl groups of glutathione confirm its presence in the glutathione-treated sample. The peak at 38 ppm suggests the presence of oxidized glutathione; this could indicate that the reduction of some species on the perovskite surface could form part of the active role of glutathione, although this remains speculative. A key function of glutathione and EDTA ligands can be inferred from their Pb-binding ability: both ligands are known to bind strongly to Pb, as shown by solution-state NMR studies (Fig. 4c, Extended Data Fig. 9, Methods).

Figure 4d shows the proposed molecular interactions of EDTA and glutathione with Pb^{2+} on the nanocrystal surface. We postulate that part of the role of these ligands is to remove undercoordinated lead from the nanocrystal surface, resulting in an electronically 'cleaner' surface with fewer defects. This 'stripping' action is consistent with the reduction in nanocrystal size upon ligand treatment, the existence of Pb–EDTA and Pb–glutathione complexes in solution, and the large binding energy of EDTA and glutathione to Pb (Extended Data Fig. 10). Some of the excess ligands could then bind to the remaining Pb on the 'cleaned' perovskite surface, further decreasing the concentration of defects.

To gain further understanding of ligand binding, we modelled the interaction of glutathione and EDTA with the $MAPbI_3$ surface using density functional theory (DFT) (Fig. 5). We consider a PbI_2-terminated surface as representative of an unpassivated perovskite surface with exposed, undercoordinated Pb atoms. We decomposed glutathione and EDTA into their possible binding moieties and calculated the binding energy of each ligand to the perovskite surface (Extended Data Fig. 10). The binding energy is defined as $E_b = E_{ligand@surface} - E_{ligand} - E_{surface}$, where the latter three terms are the energy of the surface and bound ligand, the energy of the isolated ligand, and the energy of the bare surface, respectively. Our calculated binding energy for glutathione, at −1.85 eV, is large compared to the calculated values for acetic acid (−0.58 eV) or for methylamine (−0.84 eV), which are representative of the carboxylic acid and primary amine binding moieties of glutathione. We deduce

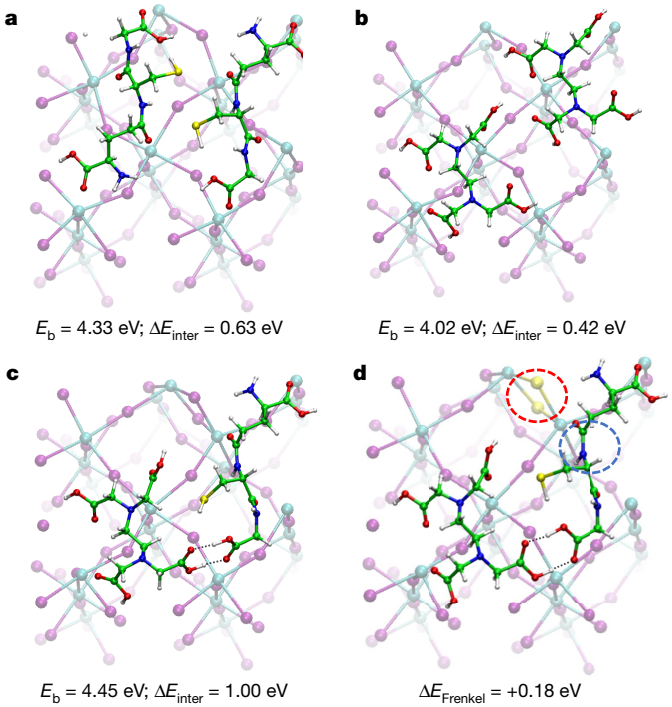

Fig. 5 | Optimized structures of interacting surface-adsorbed ligands. **a**–**c**, Optimized structures of glutathione (**a**), EDTA (**b**) and one glutathione and one EDTA molecule (**c**) on the perovskite surface along with calculated total binding energies (E_b) and their intermolecular contribution (ΔE_{inter}) in eV calculated with respect to the isolated surface-adsorbed molecules (E_b = 1.85 eV and 1.60 eV for glutathione and EDTA, respectively). **d**, Optimized structure of an iodine Frenkel defect pair (defective sites highlighted by red and blue circles) in the presence of adsorbed EDTA and glutathione. The value shown is the increase in defect formation energy compared to the unpassivated surface ($\Delta E_{Frenkel}$).

that the large binding energy is a result of contributions from multiple binding moieties. The binding energy determined for EDTA was also large (−1.60 eV), although slightly less than that of glutathione, with steric hindrance limiting binding through the tertiary amine group; this is also consistent with the observation of only glutathione in the ^{13}C solid-state NMR spectra of E+G-treated nanocrystals (Fig. 4a).

We further evaluate the binding energy of two interacting glutathione molecules, two interacting EDTA molecules, and an interacting E+G pair on the perovskite surface (Fig. 5, Extended Data Fig. 10). The E+G pair has the largest binding energy, enhanced by a synergistic effect between glutathione and EDTA; intermolecular hydrogen bonding between the carboxylic groups of glutathione and EDTA provides extra stabilization to these surface-adsorbed molecules, leading to a binding energy of −4.45 eV (Extended Data Fig. 10).

Our calculations confirm that this specific pairing of ligands has a strong affinity with the perovskite surface. We now assess how this influences the migration of halide species. Iodine Frenkel defects, which are iodide interstitial-vacancy pairs, are the most energetically probable defects at the PbI_2-terminated perovskite surface owing to their low formation energy (0.03 eV). We calculate the formation energy of an iodine Frenkel defect at the PbI_2-terminated perovskite surface in the presence of glutathione, E+G, or without passivating molecules (Methods). We find that passivation of the surface with glutathione raises the formation energy of the iodine Frenkel defects to 0.15 eV, whereas with E+G it is further increased to 0.18 eV. This is substantially higher than the calculated values for other passivating agents. For example, in the presence of polyethylene oxide, the formation of an interstitial iodine defect becomes less favourable by 0.08 eV compared to the bare perovskite surface[32]. To summarize, the large calculated binding

energy, coupled with the substantial increase in formation energy of iodide Frenkel defects, suggests that glutathione and the combination of EDTA and glutathione markedly inhibit undercoordinated Pb atoms from stabilizing these Frenkel defects[46]. Because halide Frenkel defects are expected to be the ionic species responsible for halide segregation under illumination or during device operation, our results are consistent with reduced defect formation suppressing halide segregation in E+G-treated nanocrystals.

In conclusion, we have demonstrated that treatment with a lead-complexing multidentate ligand leads to bandgap-stable red electroluminescence from mixed-halide perovskite NC-LEDs, with a maximum EQE at 620 nm of greater than 20%. We have found that stripping the nanocrystal surface of defects is an active role of these ligands. Furthermore, we have shown that both ligand–ligand and ligand–surface interactions are important to achieve a stable ligand shell on the nanocrystal surface, and that interactions of the multidentate ligand with the surface markedly suppress the formation of surface defects. Beyond light emission, this work is likely to be broadly applicable to stabilizing the bandgap of mixed-ion metal halide perovskites for a range of applications, such as multi-junction photovoltaics, and should help to expand the development of perovskites as versatile and tunable semiconductors.

Online content

Any methods, additional references, Nature Research reporting summaries, source data, extended data, supplementary information, acknowledgements, peer review information; details of author contributions and competing interests; and statements of data and code availability are available at https://doi.org/10.1038/s41586-021-03217-8.

1. Lin, K. et al. Perovskite light-emitting diodes with external quantum efficiency exceeding 20 per cent. *Nature* **562**, 245–248 (2018).
2. Xiao, Z. et al. Efficient perovskite light-emitting diodes featuring nanometre-sized crystallites. *Nat. Photonics* **11**, 108–115 (2017).
3. Zhao, X. & Tan, Z.-K. Large-area near-infrared perovskite light-emitting diodes. *Nat. Photonics* **14**, 215–218 (2020).
4. Zhao, B. et al. High-efficiency perovskite–polymer bulk heterostructure light-emitting diodes. *Nat. Photonics* **12**, 783–789 (2018).
5. Hassan, Y. et al. Facile synthesis of stable and highly luminescent methylammonium lead halide nanocrystals for efficient light emitting devices. *J. Am. Chem. Soc.* **141**, 1269–1279 (2019).
6. Draguta, S. et al. Rationalizing the light-induced phase separation of mixed halide organic–inorganic perovskites. *Nat. Commun.* **8**, 200 (2017).
7. Tian, Y. et al. Highly efficient spectrally stable red perovskite light-emitting diodes. *Adv. Mater.* **30**, 1707093 (2018).
8. Chang, J. et al. Enhanced performance of red perovskite light-emitting diodes through the dimensional tailoring of perovskite multiple quantum wells. *J. Phys. Chem. Lett.* **9**, 881–886 (2018).
9. Hassan, Y. et al. Structure-tuned lead halide perovskite nanocrystals. *Adv. Mater.* **28**, 566–573 (2016).
10. Burlakov, V. M., Hassan, Y., Danaie, M., Snaith, H. J. & Goriely, A. Competitive nucleation mechanism for $CsPbBr_3$ perovskite nanoplatelet growth. *J. Phys. Chem. Lett.* **11**, 6535–6543 (2020).
11. Wang, Z. et al. Efficient ambient-air-stable solar cells with 2D–3D heterostructured butylammonium-caesium-formamidinium lead halide perovskites. *Nat. Energy* **2**, 17135 (2017).
12. Zhou, Y. et al. Benzylamine-treated wide-bandgap perovskite with high thermal-photostability and photovoltaic performance. *Adv. Energy Mater.* **7**, 1701048 (2017).
13. Yan, J., Qiu, W., Wu, G., Heremans, P. & Chen, H. Recent progress in 2D/quasi-2D layered metal halide perovskites for solar cells. *J. Mater. Chem. A* **6**, 11063–11077 (2018).
14. Lee, D. S. et al. Passivation of grain boundaries by phenethylammonium in formamidinium–methylammonium lead halide perovskite solar cells. *ACS Energy Lett.* **3**, 647–654 (2018).
15. Zhang, X. et al. Bright perovskite nanocrystal films for efficient light-emitting devices. *J. Phys. Chem. Lett.* **7**, 4602–4610 (2016).
16. Chiba, T. et al. Anion-exchange red perovskite quantum dots with ammonium iodine salts for highly efficient light-emitting devices. *Nat. Photonics* **12**, 681–687 (2018).
17. Xiao, Z. et al. Mixed-halide perovskites with stabilized bandgaps. *Nano Lett.* **17**, 6863–6869 (2017).
18. Barker, A. J. et al. Defect-assisted photoinduced halide segregation in mixed-halide perovskite thin films. *ACS Energy Lett.* **2**, 1416–1424 (2017).
19. Meggiolaro, D., Mosconi, E. & De Angelis, F. Formation of surface defects dominates ion migration in lead-halide perovskites. *ACS Energy Lett.* **4**, 779–785 (2019).
20. Vashishtha, P. & Halpert, J. E. Field-driven ion migration and color instability in red-emitting mixed halide perovskite nanocrystal light-emitting diodes. *Chem. Mater.* **29**, 5965–5973 (2017).
21. Yang, Z. et al. Stabilized wide bandgap perovskite solar cells by tin substitution. *Nano Lett.* **16**, 7739–7747 (2016).
22. Bush, K. A. et al. Compositional engineering for efficient wide band gap perovskites with improved stability to photoinduced phase segregation. *ACS Energy Lett.* **3**, 428–435 (2018).
23. Yi, C. et al. Entropic stabilization of mixed A-cation ABX_3 metal halide perovskites for high performance perovskite solar cells. *Energy Environ. Sci.* **9**, 656–662 (2016).
24. Hu, M., Bi, C., Yuan, Y., Bai, Y. & Huang, J. Stabilized wide bandgap $MAPbBr_xI_{3-x}$ perovskite by enhanced grain size and improved crystallinity. *Adv. Sci.* **3**, 1500301 (2016).
25. Gualdrón-Reyes, A. F. et al. Controlling the phase segregation in mixed halide perovskites through nanocrystal size. *ACS Energy Lett.* **4**, 54–62 (2019).
26. Zhou, Y. et al. Composition-tuned wide bandgap perovskites: from grain engineering to stability and performance improvement. *Adv. Funct. Mater.* **28**, 1803130 (2018).
27. Abdi-Jalebi, M. et al. Maximizing and stabilizing luminescence from halide perovskites with potassium passivation. *Nature* **555**, 497–501 (2018).
28. Belisle, R. A. et al. Impact of surfaces on photoinduced halide segregation in mixed-halide perovskites. *ACS Energy Lett.* **3**, 2694–2700 (2018).
29. Zhang, L. & Sit, P. H. L. Ab initio study of the dynamics of electron trapping and detrapping processes in the $CH_3NH_3PbI_3$ perovskite. *J. Mater. Chem. A* **7**, 2135–2147 (2019).
30. Li, W., Liu, J., Bai, F.-Q., Zhang, H.-X. & Prezhdo, O. V. Hole trapping by iodine interstitial defects decreases free carrier losses in perovskite solar cells: a time-domain ab initio study. *ACS Energy Lett.* **2**, 1270–1278 (2017).
31. Meggiolaro, D. et al. Iodine chemistry determines the defect tolerance of lead-halide perovskites. *Energy Environ. Sci.* **11**, 702–713 (2018).
32. Motti, S. G. et al. Controlling competing photochemical reactions stabilizes perovskite solar cells. *Nat. Photonics* **13**, 532–539 (2019).
33. Shao, Y. et al. Grain boundary dominated ion migration in polycrystalline organic–inorganic halide perovskite films. *Energy Environ. Sci.* **9**, 1752–1759 (2016).
34. Bischak, C. G. et al. Origin of reversible photoinduced phase separation in hybrid perovskites. *Nano Lett.* **17**, 1028–1033 (2017).
35. Wu, T. et al. High-performance perovskite light-emitting diode with enhanced operational stability using lithium halide passivation. *Angew. Chem. Int. Ed.* **59**, 4099–4105 (2020).
36. Zhang, H. et al. Phase segregation due to ion migration in all-inorganic mixed-halide perovskite nanocrystals. *Nat. Commun.* **10**, 1088 (2019).
37. Flora, S. J. S. & Pachauri, V. Chelation in metal intoxication. *Int. J. Environ. Res. Public Health* **7**, 2745–2788 (2010).
38. Ferrero, M. E. Rationale for the successful management of EDTA chelation therapy in human burden by toxic metals. *BioMed Res. Int.* **2016**, 8274504 (2016).
39. Mah, V. & Jalilehvand, F. Lead(II) complex formation with glutathione. *Inorg. Chem.* **51**, 6285–6298 (2012).
40. Hayes, J. D. & Pulford, D. J. The glutathione *S*-transferase supergene family: regulation of GST and the contribution of the isoenzymes to cancer chemoprotection and drug resistance part I. *Crit. Rev. Biochem. Mol. Biol.* **30**, 445–520 (1995).
41. Zhao, Q. et al. Size-dependent lattice structure and confinement properties in $CsPbI_3$ perovskite nanocrystals: negative surface energy for stabilization. *ACS Energy Lett.* **5**, 238–247 (2020).
42. Noh, J. H., Im, S. H., Heo, J. H., Mandal, T. N. & Seok, S. I. Chemical management for colorful, efficient, and stable inorganic–organic hybrid nanostructured solar cells. *Nano Lett.* **13**, 1764–1769 (2013).
43. Richter, J. M. et al. Ultrafast carrier thermalization in lead iodide perovskite probed with two-dimensional electronic spectroscopy. *Nat. Commun.* **8**, 376 (2017).
44. Richter, J. M. et al. Enhancing photoluminescence yields in lead halide perovskites by photon recycling and light out-coupling. *Nat. Commun.* **7**, 13941 (2016).
45. Cho, C. et al. The role of photon recycling in perovskite light-emitting diodes. *Nat. Commun.* **11**, 611 (2020).
46. Bodnarchuk, M. I. et al. Rationalizing and controlling the surface structure and electronic passivation of cesium lead halide nanocrystals. *ACS Energy Lett.* **4**, 63–74 (2019).
47. Sun, Q. et al. Bright, multicoloured light-emitting diodes based on quantum dots. *Nat. Photonics* **1**, 717–722 (2007).
48. Auer-Berger, M. et al. All-solution-processed multilayer polymer/dendrimer light emitting diodes. *Org. Electron.* **35**, 164–170 (2016).
49. Yan, F. et al. Highly efficient visible colloidal lead-halide perovskite nanocrystal light-emitting diodes. *Nano Lett.* **18**, 3157–3164 (2018).

Methods

All nanocrystal syntheses were carried out under ambient conditions in a fume hood.

Materials

All chemicals were used as received without further purification. Lead iodide (PbI_2) (99.99%) was purchased from TCI Chemicals; methylammonium iodide and methylammonium bromide from Dyesol; and oleic acid (99.0%), oleylamine (70%), methylamine (MA) solution (33% in absolute ethanol), EDTA (anhydrous, ≥99%), and reduced L-glutathione (≥98.0%) from Sigma-Aldrich. All solvents, such as toluene, acetonitrile, and methyl acetate, were anhydrous and were purchased from Sigma-Aldrich. PEDOT:PSS (AI 4083), poly-TPD, and TPBi were purchased from OSM. TFB was purchased from Ossila.

Preparation of lead mixed-halide perovskite precursor

Typically, a perovskite precursor solution was prepared according to our recent work (ref. [5]), in which 922 mg of PbI_2 and 223 mg of methylammonium bromide were mixed with 4 ml of acetonitrile (ACN) and shaken to form a green–black suspension. Dry methylamine gas was bubbled through the suspension to form a compound solvent, referred to as ACN/MA, as detailed elsewhere (ref. [5]).

Synthesis of $MAPb(I_{1-x}Br_x)_3$ perovskite nanocrystals for red emission

The synthesis of the $MAPb(I_{1-x}Br_x)_3$ nanocrystals was carried out by injecting 0.2 ml of perovskite precursor dissolved in ACN/MA into toluene at 60 °C containing 2 ml of oleic acid and 0.2 ml oleylamine. The nanocrystals immediately nucleated, turning the suspension red. The reaction was continued for 1–2 min to allow for crystal growth before the nanocrystal suspension was immersed into an ice bath. We synthesized six batches of nanocrystals simultaneously, collected them into three centrifuge tubes (each containing 10 ml of nanocrystals), and the nanocrystals were iteratively precipitated by adding 20 ml of anhydrous methyl acetate. The nanocrystals were separated from excess unreacted ligands and precursors and purified by centrifugation at 8,500*g* for 10 min, then re-dispersed into 5 ml toluene. Methyl acetate (10 ml) was added to each tube and the purification process was repeated before the nanocrystals were re-dissolved in toluene to a concentration of 40 mg ml^{-1} for further characterization. These purified nanocrystals, capped with oleic acid and oleylamine, are denoted as 'neat nanocrystals'. These neat nanocrystals exhibit photoluminescence at 630 nm, and their cubic phase was confirmed by powder XRD (Fig. 2f).

Ligand treatment of $MAPb(I_{1-x}Br_x)_3$ perovskite nanocrystals

The nanocrystals underwent two washing cycles with a methyl acetate mixture, as described in the previous section. Each nanocrystal batch was dispersed in 2 ml of toluene after the washing process. Six batches of washed nanocrystals were combined to make a 12 ml (40 mg ml^{-1}) stock solution. This solution was centrifuged once more at 3,500*g* for 5 min to remove aggregates and large particles. The collected supernatant was divided into two portions: one was used as the control neat sample and the other was treated with a new ligand. Typically, 2 mmol ligand was added to 3 ml nanocrystals in toluene and stirred overnight (around 12 h) at room temperature. The unreacted ligand powder was separated from the nanocrystals after ligand treatment by centrifugation at 8,500*g* for 10 min. The collected supernatant was filtered using a PTFE syringe filter (Whatman, 0.2 μm) and stored for further characterization and device preparation.

$MAPb(I_{1-x}Br_x)_3$ nanocrystals characterization

UV–vis absorption spectra for nanocrystal solutions were recorded using a commercial Varian Cary 60 in a cuvette with a path length of 1 cm. Steady-state photoluminescence measurement of solutions was carried out with a spectrofluorometer (Fluorolog, Horiba Jobin Yvon), with a 450-W xenon lamp excitation source and a photomultiplier tube detector with an excitation wavelength of 450 nm. The absorbance spectra of $MAPb(I_{1-x}Br_x)_3$ nanocrystals films were measured using a UV–vis–near infrared spectrometer (Cary 5000, Agilent Technology). Attenuated total reflection Fourier transform infrared spectroscopy (ATR-FTIR) spectrums were obtained using FTIR spectroscopy (Cary 670, Agilent Technology). The HR-TEM images were captured using JEM-2100F (JEOL). For the TEM sample, diluted nanocrystals solutions were dropped on the copper grid with 300-mesh carbon film. The XPS results were obtained using a spectrometer (ESCALAB 250Xi, Thermo Fisher Scientific) with a monochromatic Al–Kα X-ray source. The confocal photoluminescence images and spectra were obtained using a laser scanning confocal microscope (LSM 780 NLO, Zeiss). The ultraviolet photoemission spectra were carried out using an AXIS Nova (Kratos Analytical) with a He (21.2 eV) ultraviolet source.

Transient absorption spectroscopy of $MAPb(I_{1-x}Br_x)_3$ nanocrystals

A Ti:sapphire laser (Coherent Astrella) operating at 1 kHz pumped an optical parametric amplifier (Light Conversion, Topas Prime Plus) to generate 520-nm pump pulses. The 800-nm fundamental was used to generate white light probe pulses in a sapphire plate. The pump pulse energy in TAS was 106 μJ cm^{-2}. The broadband probe pulse energies were 124 μJ cm^{-2} and 146 μJ cm^{-2} for the E+G-treated and neat nanocrystal films, respectively. Transient absorption spectra were collected using an instrument constructed in-house, with 100-fs time resolution and pump–probe time delays of up to 800 ps. The TAS signal at alternate time delays was collected in ascending order, and the signal at the remaining time delays in descending order, to ensure that any changes in the sample during the scan were not systematically encoded into the transient. Each scan required 50 s. For each film, 72 TAS spectra were measured before 30 s of exposure to a 405-nm continuous-wave laser with the power density set at 7.09 W cm^{-2}. The 405-nm laser also acted as the excitation source for the measurement of fluorescence spectra. Fluorescence was collected through a fibre optic cable (Thorlabs M53L01) by a portable spectrometer (Ocean Optics, Flame-T). After completing the exposure, the TAS instrument was initialized, a process that requires 40 s. TAS scans were then collected, with a few seconds of exposure to the 405-nm continuous-wave laser before and after each scan to compensate for the recovery of the halide migration during the TAS scan. This procedure was repeated for 60 TAS scans (Extended Data Fig. 3).

Absorbance, fluorescence and TAS measurements were performed on oleic acid/oleylamine-capped and E+G-capped nanocrystals in spin-cast encapsulated films. The average wavelength of the fluorescence immediately before and after each TAS scan was used to estimate the average fluorescence wavelength during the scan. This estimates the average amount of halide segregation over 60 TAS scans. The duration of exposure to the 405-nm light after each scan was set to minimize the change in the average fluorescence wavelength during the 60 TAS scans, shown in Extended Data Fig. 3. TAS measurements were performed on different spots on each film using different durations of 405-nm exposure between TAS scans until a small standard deviation in the average fluorescence wavelength was achieved. This indicated that, with this additional irradiation, the nanocrystals did not undergo further halide segregation nor recovery of segregation during the 60 TAS scans.

Time-resolved photoluminescence spectra measurement

The time-resolved photoluminescence spectra of the $MAPb(I_{1-x}Br_x)_3$ nanocrystals were measured using a fluorescence lifetime spectrometer (Fluo Time 300, PicoQuant). The samples were photoexcited using a 450-nm diode laser head (LDH-D-C-450, PicoQuant) coupled to a PDL 820 laser drive. The photons emitted from the nanocrystals were collected using a PicoHarp TCSPC module with a photomultiplier detector and monochromator (PMA-C 182-N-M).

Estimation of the EQE limit

Our observed EQE of greater than 20% seems to be the limit of what is feasible when considering optical outcoupling efficiencies from perovskite thin films in LED device structures[4]. However, the precise outcoupling efficiency depends strongly upon the refractive index of the emission layer, and furthermore, photon recycling can contribute to enabling waveguided light to be reabsorbed and externally emitted from the device. To quantify this in more detail, we first estimated the refractive index of our nanocrystal films using spectroscopic ellipsometry as $n \approx 1.82$ at 620 nm. Considering a thin film on glass, with $n = 1.82$, and accounting for emission from both the perovskite–air and perovskite–glass interfaces, we determine an outcoupling efficiency of 32.4%. Our observations of a PLQY of 70% for such films is clearly in excess of this, but can be understood by accounting for photon recycling, following the procedure in ref. [44]. For our films, with an outcoupling efficiency of 32.4% and an external PLQY of 70%, we estimate an internal PLQY of 87.8% (further details are shown in the calculation below). For the LEDs, this calculation is slightly more complicated because there are a larger number of material layers, there is a reflective rear electrode, and parasitic absorption can occur in the charge-injection layers and in the electrode materials[45]. However, detailed calculations have been made for organic light-emitting diodes with very similar device stacks and refractive indices of the materials used, including the emission layer at $n \approx 1.8$. Putting our internal PLQY of 87.8% into the average calculated escape cone efficiencies in ref. [50] results in an estimated EQE for electroluminescence of 27%. Therefore, our measured EQE of 20% is entirely feasible.

Details of the internal PLQY calculation

See also ref. [44]. The PLQY of a perovskite film coated upon a glass slide is measured in an integrated sphere. The light is isotopically emitted within the perovskite film, and a certain fraction emitted within a specific solid angle will escape from the front and back surface of the film, with a considerable fraction of the light totally internally reflected and reabsorbed in the plane of the film. Because the overlap of emission and absorption spectra is considerable for these perovskite materials, we estimate that within a few tens of micrometres, more than 90% of the waveguided light will be reabsorbed and therefore very little light will be emitted from the edges of perovskite film coated on the 2 × 2 cm glass slides. The analysis that we set out below, which includes realistic parameters, determines the relationship between measured PLQY and internal PLQY. The probability for a photon that is isotopically emitted from within one medium to be transmitted through an interface between the medium within which it was emitted and the adjacent medium, with refractive indices n_1 and n_2, respectively, can be estimated as

$$n_{\text{trans}} = \frac{\Omega_{\text{esc}}}{4\pi} T \approx \frac{n_2^3}{n_1(n_1+n_2)^2}$$

where Ω_{esc} is the escape solid angle and T is the transmittance. Ellipsometry measurements estimate the refractive index of perovskite nanocrystal films to be around 1.82 at 620 nm. Taking the refractive indices of air, glass and the perovskite nanocrystal film to be 1, 1.5 and 1.82, respectively, using the above equation we estimate the probability for a photon to be transmitted through the perovskite–air interface to be 6.9% and through the perovskite–glass interface to be 16.8%.

We assume the optical density of the nanocrystal films to be 0.02 at the photoluminescence emission wavelength of 620 nm (or 2 eV). Before reaching an interface, photons will, on average, have travelled through an optical density of 0.01. Of the total photons emitted, 16.8% of the photons will be travelling towards the perovskite–glass interface within the escape cone, and 6.9% of the photons will be travelling towards the perovskite–air interface within the escape cone. The photons emitted towards the perovskite–air interface, but within the solid angle in between the perovskite–air and the perovskite–glass escape cones (which accounts for 16.8 − 6.9% = 9.9% of the photons), will be reflected off the perovskite–air interface, and will then escape out of the perovskite–glass interface. Therefore, accounting for the small attenuation due to self-absorption, the total escape probability for the perovskite nanocrystal films is estimated to be:

$$\eta_{\text{esc}} = 10^{-0.01} \times (16.8\% + 6.9\% + 10^{-0.02} \times (16.8\% - 6.9\%)) = 32.4\%$$

Following equation 3 in ref. [44], the relation between the internal PLQY (η) and the measured PLQY (η_{ext}) is given by:

$$\eta_{\text{ext}} = \frac{(\eta \times \eta_{\text{esc}})}{1 - \eta + (\eta \times \eta_{\text{esc}})}$$

Substituting the measured external PLQY of 70% ($\eta_{\text{ext}} = 0.70$) and the total escape probability of 32.4%, ($\eta_{\text{esc}} = 0.324$), we obtain an internal PLQY η of 0.878 or 87.8%. We note that this expression accounts for the photon recycling and illustrates that the external measured PLQY can deviate considerably from the internal PLQY.

ICP-MS analysis

To provide evidence of the 'stripped' Pb–ligand complex (where the ligand is EDTA or glutathione) in the sediment, we analysed the resulting precipitates (which includes the potential Pb–ligand complex and undissolved ligand) by inductively coupled plasma mass spectrometry (ICP-MS) after repeated washing with toluene (10 times). As both EDTA and glutathione have very low solubility in toluene, this process effectively disperses and removes the remaining nanocrystals while retaining the Pb–ligand complexes in the residue. To rule out the lead content arising from any remaining nanocrystals, the toluene supernatant from the final washing step was also subjected to ICP-MS analysis. The results show lead is present in the precipitate at the following concentrations: glutathione-treated samples (518 μg mg^{-1}) > E+G-treated samples (428 μg mg^{-1}) > EDTA-treated samples (354 μg mg^{-1}) compared with a concentration of nearly 0 ug mg^{-1} in the final supernatant. To estimate whether EDTA and glutathione have different Pb^{2+}-complexation abilities, we calculated the binding energy between the two ligands and a Pb^{2+} ion (Extended Data Fig. 10). The complexes have a hemidirected coordination geometry, and EDTA has a considerably greater binding energy (by 0.80 eV) to Pb^{2+} than does glutathione.

Fabrication and characterization of $MAPb(I_{1-x}Br_x)_3$ NC-LEDs

Our final device stack, for which a schematic and an SEM cross-sectional image are shown in Fig. 3a, b, includes a 'triple-layer' hole-injection layer, comprising PEDOT:PSS, poly-TPD and the deep work-function polymer (TFB), followed by a thin dense layer of the perovskite nanocrystals (around 30 nm), capped with the electron transport layer of TBPi and a lithium fluoride/aluminium cathode. Typically, ITO-coated glass substrates were cleaned by an ultra-sonification process in deionized water, acetone and isopropanol for 10 min. PEDOT:PSS was spin-coated onto an ITO substrate at 5,000 rpm for 40 s. The coated substrates were transferred to an N_2-filled glove box and annealed at 140 °C for 10 min. Poly-TPD solution (15 mg ml^{-1}) in chlorobenzene and TFB solution (20 mg ml^{-1}) in *p*-xylene were sequentially spin-coated onto the substrates at 4,000 rpm for 40 s. Each layer was annealed at 140 °C for 30 min. The $MAPb(I_{1-x}Br_x)_3$ nanocrystals were spin-coated onto the substrates at 2,000 rpm for 40 s. A layer of TPBi (70 nm), LiF (1 nm) and Al (80 nm) were sequentially deposited using a thermal evaporation system. The fabricated NC-LEDs were characterized using Keithley 2400 source measurement unit and a Minolta CS 2000 spectroradiometer. NC-LEDs were encapsulated with glass and measured under ambient conditions. The cross-sectional images of NC-LEDs were obtained using SEM (SU8220 FE-SEM, Hitachi) with an accelerating voltage of 10 kV.

Solid-state ^{13}C NMR

Solid-state ^{13}C magic-angle spinning NMR was performed at 9.4 T (KBSI Western Seoul Center) using a 4 mm Bruker triple resonance probe. The prepared nanocrystals were packed into reduced-volume zirconia rotors under a nitrogen atmosphere and were spun at 8 kHz. ^{13}C data were acquired using a ^{1}H–^{13}C Hartmann–Hahn cross-polarization sequence with 100 kHz SPINAL64 ^{1}H decoupling.

Solution ^{1}H NMR

To assess the interaction between the ligands and Pb^{2+}, we measured ^{1}H NMR spectra of the ligands mixed with PbI_2. Figure 4a shows annotated structural diagrams of the ligands, indicating the different moieties responsible for the NMR resonances and the different binding units present in glutathione, namely glutamine (Glu), cysteine (Cys) and glycine (Gly). In Fig. 4c and Extended Data Fig. 9, we show that both ^{1}H signals from EDTA shift downfield and broaden, indicating multidentate complexation of EDTA to Pb^{2+}. We mixed glutathione and PbI_2 in d_6-DMSO and observed two changes: considerable broadening and increased chemical shifts of the cysteinyl β_{cys} resonance; and decreased chemical shifts of the amide NH_{cys} resonances. The first change indicates that Pb^{2+} binds to cysteinyl sulfur[39,51]. The shift of amide NH_{cys} resonances is probably caused by the proximity of the amide NH to the Pb^{2+}, as is seen when the chemically similar Cd^{2+} binds to glutathione[52]. We also observe a weakening of the geminal ^{2}J coupling of the glutamine beta protons (β_{glu}), indicating that the COOH is also bound to Pb^{2+}. The alpha proton of glycine (α_{gly}) displayed no observable shift upon the addition of PbI_2, in agreement with previous work showing that the COO^- group of glycine does not bind to Pb^{2+} (ref. [53]). In Extended Data Fig. 9 we show the ^{1}H NMR spectra when both ligands (E+G) are mixed with PbI_2. We observe that all of the changes associated with interactions that are present in the solutions containing the individual ligands are also present in the solution of the combined ligands, indicating that when both ligands are combined in the E+G mixture they maintain their individual interactions with PbI_2. We show the proposed molecular interactions of the E+G ligands with Pb^{2+} on the nanocrystal surface in Fig. 4d. We conclude that, in this system, EDTA and glutathione can coordinate with Pb^{2+} via the aforementioned binding groups.

DFT approach

We modelled the interaction of glutathione and EDTA on perovskite surfaces using the state-of-the-art DFT calculations, including dispersion interactions, to mimic the surface chemistry of perovskite nanocrystals. Owing to the uncertain nature of surfaces and their terminations in mixed-halide perovskites, we focus here on $MAPbI_3$ for which we have a reliable surface picture. We evaluate in due course the possible effect on the results of considering a single halide in place of a mixed halide. All our results are obtained considering a PbI_2-terminated surface, which is representative of the extreme situation of a fully unpassivated perovskite surface exposing undercoordinated surface Pb.

The calculations were run with the following assumptions. First, halide demixing is triggered by defect formation and/or migration. Second, most defects and migration channels are on surfaces, so surface passivation blocks defect formation, ion migration and demixing. Third, surface passivation molecules should bind effectively to the perovskite surface and pack tightly, thus being an effective migration blocker. We considered the adsorption of single glutathione and EDTA molecules, and then considered glutathione–glutathione, EDTA–EDTA and glutathione–EDTA coadsorption.

Because glutathione is quite a complex molecule, we initially investigated which chemical fragment within glutathione interacts most strongly with the perovskite surface. Thus, we decomposed glutathione and EDTA into their possible binding moieties and calculated the binding energy of the fragments with the perovskite (Extended Data Fig. 10). The binding energy is defined as $E_b = E_{molecule@surface} - E_{molecule} - E_{surface}$.

The results show that the amidic fragment of glutathione is the most strongly binding one; see Extended Data Fig. 10. Typically, the calculated binding energy of glutathione is large (−1.85 eV), arising from a partial sum of all binding moieties. EDTA shows a reduced binding energy to perovskite compared with glutathione (−1.60 versus −1.85 eV), with EDTA mainly binding through carboxylic groups. Although the tertiary aminic groups may show a greater binding energy to Pb than does COOH (Extended Data Fig. 10), steric hindrance prevents EDTA from exploiting such interactions.

To evaluate the energetics of forming a compact monolayer on the perovskite surface, thus effectively blocking all possible undercoordinated Pb atoms acting as defect-nucleating centres, we next evaluated the binding energies of two interacting glutathiones, two interacting EDTA molecules, and an interacting E+G pair on the perovskite surface. In the case of two or more interacting molecules, the binding energy includes both surface–molecule and molecule–molecule interactions. The E+G pair was found to have the greatest binding energy, enhanced by a synergistic effect between glutathione and EDTA. Intermolecular hydrogen bonding between carboxylic groups of the glutathione and EDTA provides extra stabilization to these surface-adsorbed molecules, leading to a binding energy of −4.45 eV (Extended Data Fig. 10).

To connect the calculated binding energies to the defect-blocking properties of the respective surface-adsorbed molecules, we considered the energetics of formation of an iodine Frenkel defect pair (that is, iodine vacancy/interstitial iodine) at the surface. These defects are the energetically most probable defects at the PbI_2-terminated perovskite surface; thus, they constitute a case study to evaluate the effect of surface-adsorbed molecules on defect formation energies. We thus calculated the formation energy of an iodine Frenkel defect pair at the PbI_2-terminated perovskite surface without passivating molecules and in the presence of glutathione and E+G.

Formation of an iodine Frenkel defect on the PbI_2-terminated perovskite surface has very low formation energy (0.03 eV), in line with the instability of the unpassivated surface (complete surface passivation by methylammonium iodide raises the formation energy to 0.84 eV). Surface passivation by glutathione raises the formation energy to 0.15 eV, with passivation by E+G further raising it to 0.18 eV. This clearly demonstrates the blocking of surface defects by glutathione and the synergistic effect of E+G. To put this value into context, when modelling the interaction of polyethylene oxide (PEO) with the same perovskite surface, we calculated an increase in defect-formation energy of 0.08 eV for a complete monolayer of CH_3OCH_3 (mimicking PEO). The values obtained here for glutathione and E+G are therefore to be considered as very high.

To sum up, we have evaluated the binding of glutathione, EDTA and E+G on the perovskite surface and evaluated their ability to block Frenkel defects. The results show a synergistic effect of E+G, to deliver the highest surface binding energy and the highest defect-blocking activity. The key to efficient surface passivation is the concurrent action of strong molecule–surface and molecule–molecule interactions.

All simulations were carried out with the Quantum Espresso program package[53]. DFT calculations were carried out on the (001) $MAPbI_3$ surface within the supercell approach by the Perdew–Burke–Ernzerhof (PBE)[54] functional using ultrasoft pseudopotentials (shells explicitly included in calculations: I 5*s*, 5*p*; N, C 2*s*, 2*p*; O 2*s*, 2*p*; H 1*s*; Pb 6*s*, 6*p*, 5*d*; S 3*s*, 3*p*) and a cutoff on the wavefunctions of 25 Ryd (200 Ryd on the charge density). DFT-D3 dispersion interactions were included in the calculation[54].

Slab models were built starting from the tetragonal phase of $MAPbI_3$ (ref. [55]) by fixing cell parameters to the experimental values and generating a 2×2 supercell in the *a* and *b* directions. Along the non-periodic direction perpendicular to the slabs, 10 Å of vacuum was added in all cases. A symmetric disposition of the organic cations on the external layers of the slabs was adopted in all cases, leading to supercells with zero average dipole moments. Such an arrangement of organic

cations provided a flat electrostatic potential in the vacuum region of the supercells for all modelled slabs.

Data availability

The data that support the findings of this study are available from the corresponding authors upon reasonable request.

Code availability

Computational codes used in this work are available from the corresponding authors upon reasonable request.

50. Salehi, A., Chen, Y., Fu, X., Peng, C. & So, F. Manipulating refractive index in organic light-emitting diodes. *ACS Appl. Mater. Interfaces* **10**, 9595–9601 (2018).
51. Sisombath, N. S. & Jalilehvand, F. Similarities between *N*-acetylcysteine and glutathione in binding to lead(II) ions. *Chem. Res. Toxicol.* **28**, 2313–2324 (2015).
52. Delalande, O. et al. Cadmium–glutathione solution structures provide new insights into heavy metal detoxification. *FEBS J.* **277**, 5086–5096 (2010).
53. Giannozzi, P. et al. QUANTUM ESPRESSO: a modular and open-source software project for quantum simulations of materials. *J. Phys. Condens. Matter* **21**, 395502 (2009).
54. Perdew, J. P., Burke, K. & Ernzerhof, M. Generalized gradient approximation made simple. *Phys. Rev. Lett.* **77**, 3865–3868 (1996).
55. Poglitsch, A. & Weber, D. Dynamic disorder in methylammoniumtrihalogenoplumbates(II) observed by millimeter-wave spectroscopy. *J. Chem. Phys.* **87**, 6373–6378 (1987).

Acknowledgements This work was partially funded by the Engineering and Physical Sciences Research Council (EPSRC) UK through grants EP/M005143/1 and EP/M015254/2. This work is part of the PEROCUBE project, which has received funding from the European Union's Horizon 2020 research and innovation program under grant agreement no. 861985. Y.H., A.S., R.S., H.J.S. and R.H.F. acknowledge funding and support from the SUNRISE project (EP/P032591/1), funded by the EPSRC. A.S. and R.H.F. acknowledge support from the UKIERI project. A.S. acknowledges funding and support from DST, Pratiksha Trust, IISc and MHRD. R.S. acknowledges a Newton International Fellowship from The Royal Society. M.L.C. acknowledges financial support from the Achievement Rewards for College Scientists (ARCS) Foundation, Oregon Chapter. This study was partially supported by the National Research Foundation of the Republic of Korea (NRF-2018R1C1B6005778, 2018R1A2B2006198, 2020R1A4A1018163 and 2019R1A6A1A10073437) and the Materials Innovation Project (NRF-2020M3H4A3081793) funded by the National Research Foundation of Korea. NMR data were acquired on a 400-MHz solid-state NMR spectrometer (AVANCE III HD, Bruker) at KBSI Western Seoul Center. The HR-TEM, XPS, NMR, confocal photoluminescence and SEM experiments were supported by UNIST Central Research Facilities (UCRF). J.H.P. thanks A. Lee for assistance with TEM. Y.H. thanks M. Danie for assistance with TEM; S. M. Rabea, T. S. Ibrahim, A. M. Ali and T. Janes for assistance with NMR analysis; and M. N. Ahmed for advice on Fig. 1. We thank B. Wenger for discussions concerning the use of EDTA as a ligand in perovskite nanocrystals. Y.H. thanks A. Marshall and J. Sahmsi for discussions concerning the FTIR and N. Sakai for discussing XRD results. We thank V. Burlakov and S. Mahesh for discussions concerning the halide-segregation mechanism. Y.H. acknowledges funding and support from Linguistix Tank Inc. (LXT AI), Canada.

Author contributions Y.H. initiated the project, synthesized the nanocrystals, conceived the multidentate-ligand approach, developed and performed the ligand treatment process and, with J.H.P., performed the TEM, UV–vis absorption, photoluminescence and XRD measurements. Y.H., A.S. and H.J.S. planned the experiments and overall project targets. Y.H. coordinated the collaboration efforts and was assisted by A.S. J.H.P. fabricated LED devices. A.S. assisted with the synthesis of the nanocrystals and performed the PLQY and photothermal deflection spectroscopy measurements. R.S. assisted with the PLQY and photothermal deflection spectroscopy measurements. Y.H., M.L.C., M.J., C.Y. and J.L. performed the NMR experiments and analysed the data. J.H.P. performed STEM experiments and Y.H. analysed the data. J.H.P. and B.R.L. assisted with the characterization of the materials and the LEDs. M.H.S., H.C., S.H.P. and B.R.L. provided support for the characterization of the materials and devices. J.H.P. and B.R.L. carried out the device-stability tests. M.L.C. and J.C.S. designed and executed the TAS experiments and M.L.C. performed data analysis. E.M., E.R. and F.D.A. conducted the computational simulations. C.Y.W., B.R.L., R.H.F. and H.J.S. supervised the work undertaken in their laboratories. Y.H. drafted the first version of the manuscript, with assistance from J.C.S., C.Y.W. and H.J.S. All authors have read and commented upon, or contributed to the writing of, the manuscript.

Competing interests H.J.S. is a co-founder of Oxford PV, which is commercializing perovskite-based photovoltaics. H.J.S. and R.H.F. are co-founders of Helio Display Materials, which is commercializing perovskite materials for light-emitting applications.

Additional information
Correspondence and requests for materials should be addressed to Y.H., C.Y.W., B.R.L. or H.J.S.

Peer review information *Nature* thanks Chih-Jen Shih and the other, anonymous, reviewer(s) for their contribution to the peer review of this work.

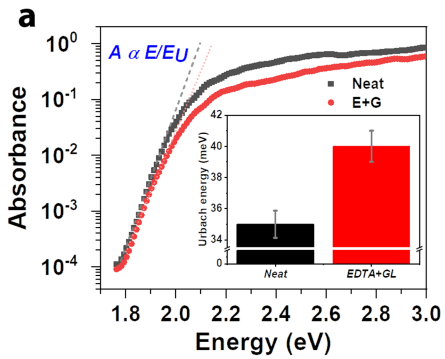

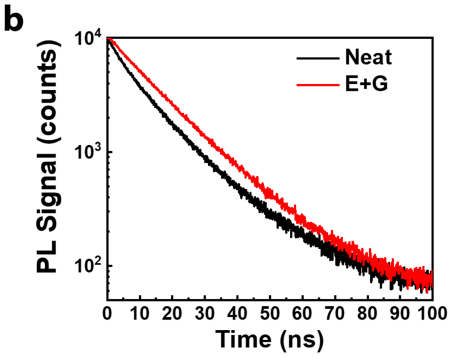

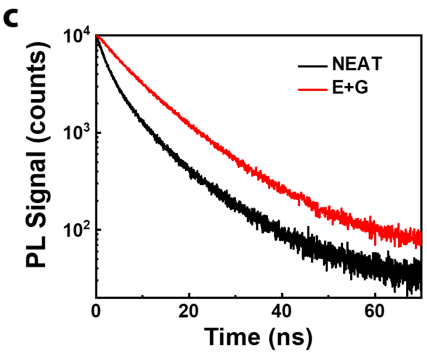

d

Condition	t_{avr} [ns]	t_1 [ns]	t_2 [ns]	c^2
Neat_solution	11.90	7.46 (56.18%)	17.61 (43.82%)	1.19
E+G_solution	14.52	9.86 (33.08%)	16.81 (66.92%)	1.05
Neat_film	5.28	2.87 (69.42%)	10.76 (30.58%)	1.38
E+G_film	9.31	5.89 (51.03%)	12.87 (48.97%)	1.04

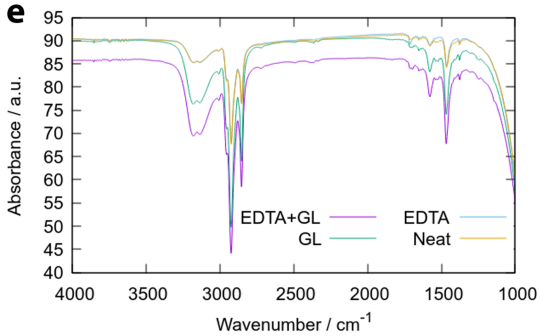

f

Sample	Neat	EDTA	GL	EDTA+GL
Iodine: PP At. % [halide ratio]	3.37 [41.3%]	3.56 [39.9%]	3.71 [40.5%]	3.59 [38.1%]
Bromine: PP At. % [halide ratio]	4.79 [58.7%]	5.36 [60.1%]	5.44 [59.5%]	5.83 [61.9%]
Lead (Pb): PP At. %	1.42	1.55	1.53	1.51

Extended Data Fig. 1 | Characteristics of neat nanocrystals and nanocrystals with ligand treatment. a, Photothermal deflection spectra of neat perovskite nanocrystal films and E+G-treated nanocrystal films deposited on quartz substrates. The inset shows the calculation of the average Urbach energy for these two samples. **b**, **c**, Time-resolved photoluminescence decay of neat nanocrystals and E+G-treated nanocrystals, as a solution dispersed in toluene (**b**) and as films (**c**). **d**, The corresponding time-resolved photoluminescence lifetimes of the neat nanocrystals and the E+G-treated nanocrystals. **e**, FTIR spectra of drop-cast films from nanocrystals synthesized in oleic acid. neat and after treatment with EDTA, glutathione or E+G. **f**, XPS of nanocrystals before and after ligand treatment, showing that the ligand-treated nanocrystals approximately correspond to $MAPb(I_{0.4}Br_{0.6})_3$, whereas the neat nanocrystals were synthesized using the composition of $MAPb(I_{0.67}Br_{0.33})_3$.

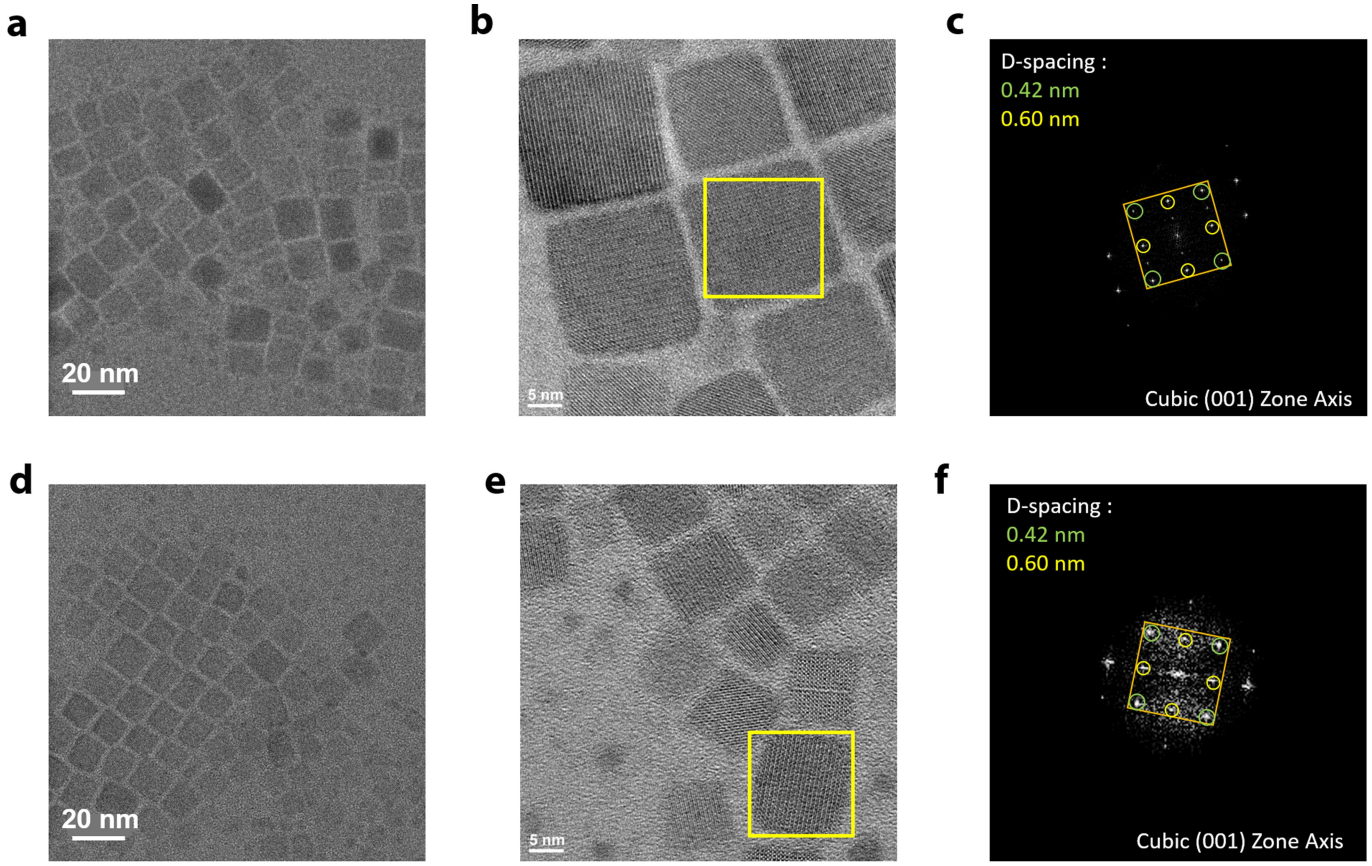

Extended Data Fig. 2 | HR-TEM images of nanocrystals. a, **b**, HR-TEM images of neat nanocrystals at different magnifications. **c**, Fast Fourier transformation of the selected region in **b**, in which the interplanar lattice spacing of the cubic phase is 0.60 and 0.42 nm for the {001} and {110} family of planes. **d**, **e**, HR-TEM images of E+G-treated nanocrystals at different magnifications. **f**, Fast Fourier transformation of the selected region in **e** showing a similar cubic structure to neat nanocrystals.

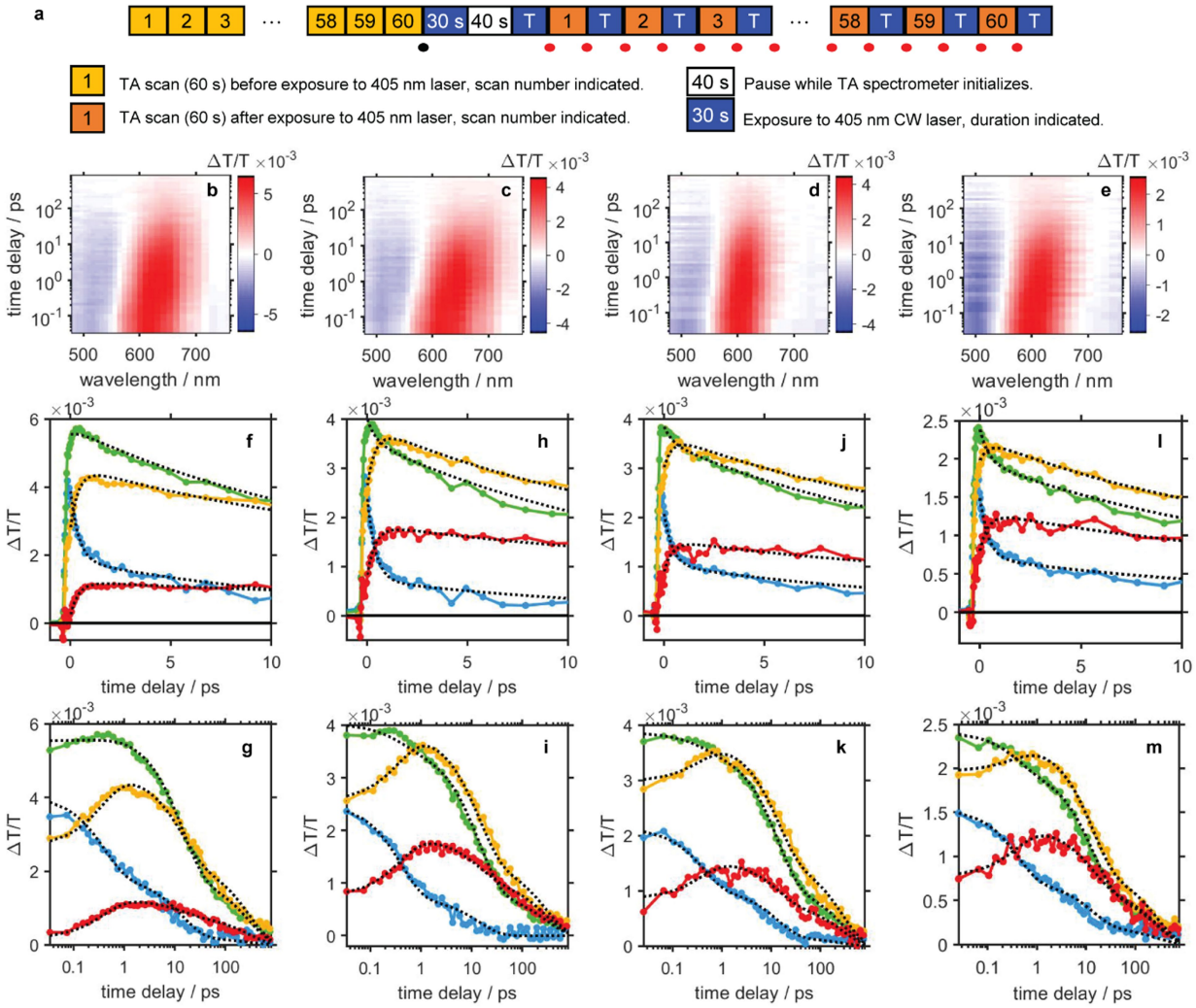

n

	Neat	E+G capped
Fit amplitudes	Figure 2g	Figure 2h
Blue component	0.40±0.02 ps (0.40±0.01 ps)	0.41±0.04 ps (0.41±0.01 ps)
Green component	13.8±0.7 ps (13.8±0.6 ps)	13.5±1.0 ps (13.5±1.1 ps)
Red component	288±16 ps (286±18 ps)	276±26 ps (276±26 ps)

Extended Data Fig. 3 | Effect of ligands on nanocrystal excited-state dynamics. a, Schematic of TAS procedure. Coloured circles represent photoluminescence measurements before (black) and after (red) illumination with a 405-nm laser. Periodic re-exposure of the sample to the 405-nm laser maintained a stable photoluminescence wavelength during TAS scans without causing additional segregation. The duration of the re-exposure, *T*, was 10 s and 3 s for neat and E+G treated nanocrystals, respectively. For neat nanocrystals, the photoluminescence wavelength was initially 649 nm and was 669 ± 1 nm after exposure; the photoluminescence of E+G-treated nanocrystals was initially 628 nm and was 632 ± 1 nm after exposure. **b**–**e**, TAS of neat (**b**, **c**) and E+G-treated (**d**, **e**) nanocrystals before (**b**, **d**) and after (**c**, **e**) illumination. **f**–**m**, Transients of neat (**f**–**i**) and E+G-treated (**j**–**m**) nanocrystals before (**f**, **g**, **j**, **k**) and after (**h**, **i**, **l**, **m**) illumination. Traces are average signal in wavelength ranges chosen to highlight wavelength-dependent dynamics. Blue, green, yellow and red traces for the neat nanocrystals and the E+G-treated nanocrystals correspond to 560–600 and 550–580 nm, 600–640 and 580–610 nm, 640–680 and 610–640 nm, 680–720 and 640–670 nm, respectively. Black dashed lines are a global fit to a tri-exponential function. **n**, Time constants before (after) illumination of each nanocrystal sample, found by a global fit of transient absorption spectra. Colours refer to those in Fig. 2g, h.

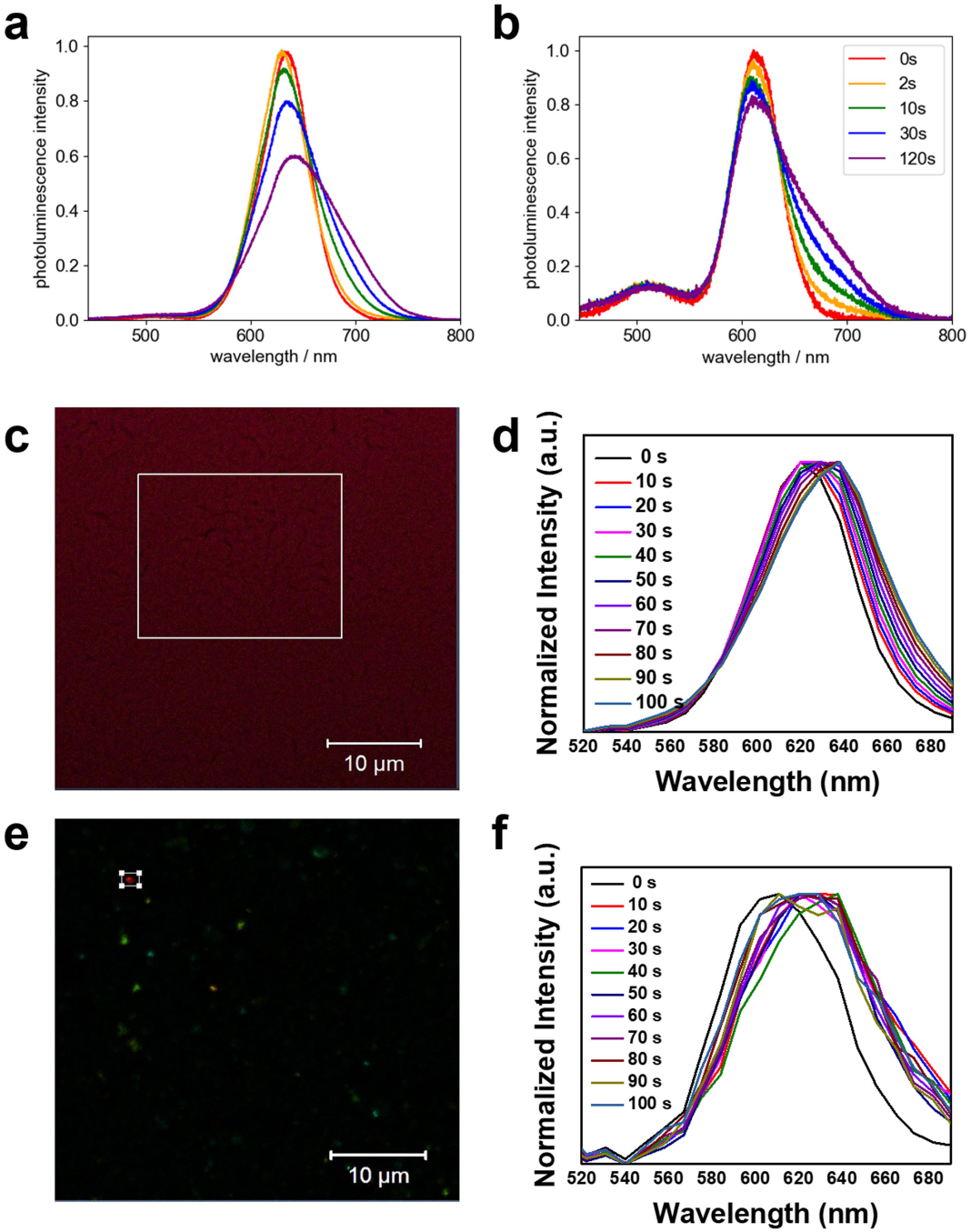

Extended Data Fig. 4 | Halide segregation in diluted neat nanocrystals. **a**, **b**, Normalized photoluminescence spectra of spin-cast films of neat nanocrystals and polymethyl methacrylate (PMMA), in a nanocrystal:PMMA mass ratio of 1.03 (**a**) and 0.006 (**b**). A 405-nm continuous-wave laser was used as an excitation source and caused halide segregation, with the duration of irradiation indicated in the legend. The redshifted shoulder that developed during irradiation is ascribed to the recombination from within an iodide-enriched minority phase with a smaller bandgap. This shoulder showed no dependence on the nanocrystal concentration in the film, indicating that segregation can occur in isolated nanocrystals. **c**, **d**, Confocal photoluminescence images (**c**) and normalized photoluminescence spectra (**d**) of spin-cast films of neat nanocrystals over time under constant excitation with a 405-nm continuous-wave laser. The photoluminescence spectra were obtained from the highlighted region of **c**. **e**, **f**, Confocal photoluminescence images (**e**) and normalized photoluminescence spectra (**f**) of spin-cast films of neat nanocrystals and PMMA, in a nanocrystal:PMMA mass ratio of 0.001 over time under constant excitation with a 405-nm diode laser. The photoluminescence spectrum was obtained from the highlighted region of **e**.

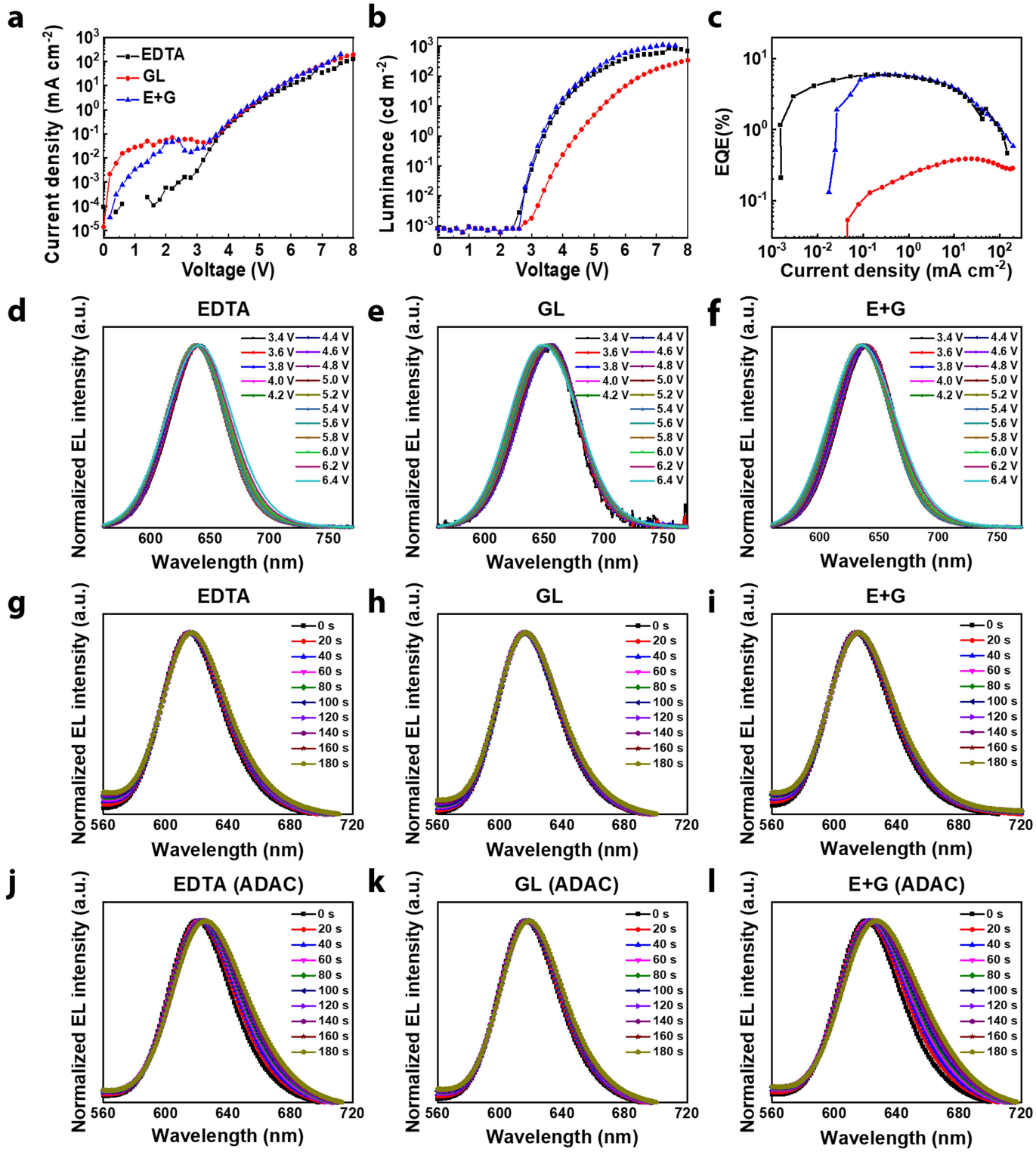

Extended Data Fig. 5 | Stability of the electroluminescence spectra of the mixed-halide $MAPb(I_xBr_{1-x})_3$ NC-LEDs with different ligand treatments. **a**–**c**, Current density–voltage (*J*–*V*) curves (**a**), luminance–voltage (*L*–*V*) curves (**b**) and EQE–current density curves (**c**) of NC-LEDs with different ligands treatment. **d**–**f**, Electroluminescence spectra of EDTA-treated (**d**), glutathione-treated (**e**) and E+G-treated (**f**) NC-LEDs at different bias voltages. **g**–**i**, Electroluminescence spectra of EDTA-treated (**g**), glutathione-treated (**h**) and E+G-treated (**i**) NC-LEDs over time at a constant current density of 10 mA cm^{-2}. **j**–**l**, Electroluminescence spectra after treatment of the EDTA-treated (**j**), glutathione-treated (**k**) and E+G-treated (**l**) NC-LEDs with 1-adamantanecarboxylic acid (ADAC), measured over time at a constant current density of 10 mA cm^{-2}.

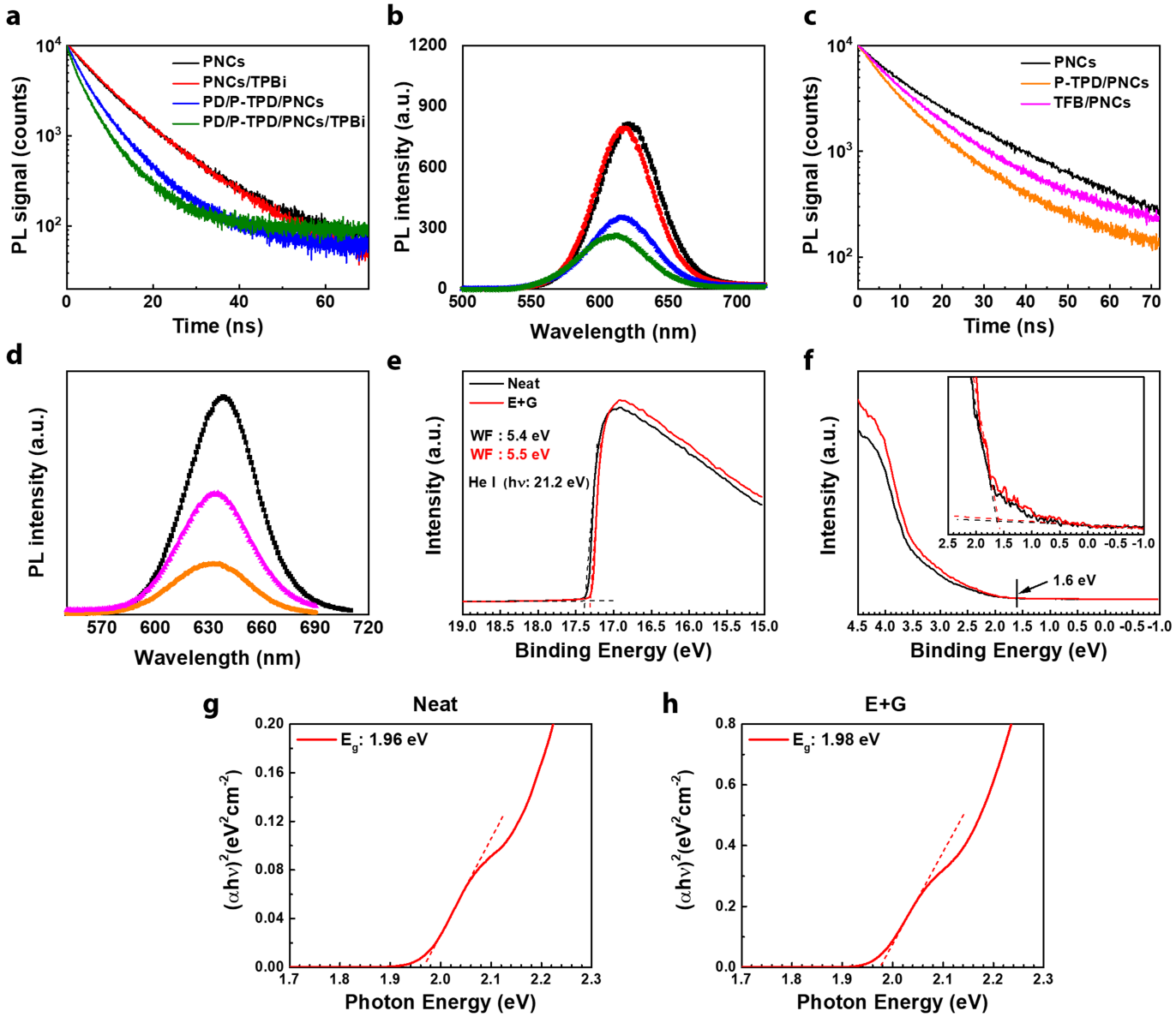

Extended Data Fig. 6 | Characteristics of nanocrystal films with different charge-transporting layers. a, Time-resolved photoluminescence decays of E+G-treated nanocrystal films with various charge-transporting layers (excitation at 450 nm). PNCs, perovskite NCs; PD, PEDOT:PSS; P-TPD, poly-TPD. **b**, Photoluminescence intensities of E+G-treated nanocrystal films with various charge-transporting layers (excitation at 350 nm). Photoluminescence decays considerably faster, and photoluminescence intensity is reduced, in the presence of a poly-TPD HTL, whereas little change is observed with a TPBi ETL. This shows that exciton quenching markedly affects the interface between poly-TPD and the nanocrystals, resulting in a deterioration of device efficiency. **c**, Time-resolved photoluminescence decays of E+G-treated nanocrystal films with various HTLs (excitation at 450 nm). **d**, Photoluminescence intensities of E+G-treated nanocrystal films with various HTLs (excitation at 450 nm). TFB HTLs have longer photoluminescence decays and larger photoluminescence intensity compared to the poly-TPD HTLs, indicating that there is less exciton quenching at the interface between the nanocrystals and the TFB HTLs. **e**, **f**, Photoemission cutoff energy (**e**) and the valence-band region (**f**) of neat and E+G-treated nanocrystals from ultraviolet photoemission spectra. **g**, **h**, Optical bandgaps of neat nanocrystals (**g**) and E+G-treated nanocrystals (**h**).

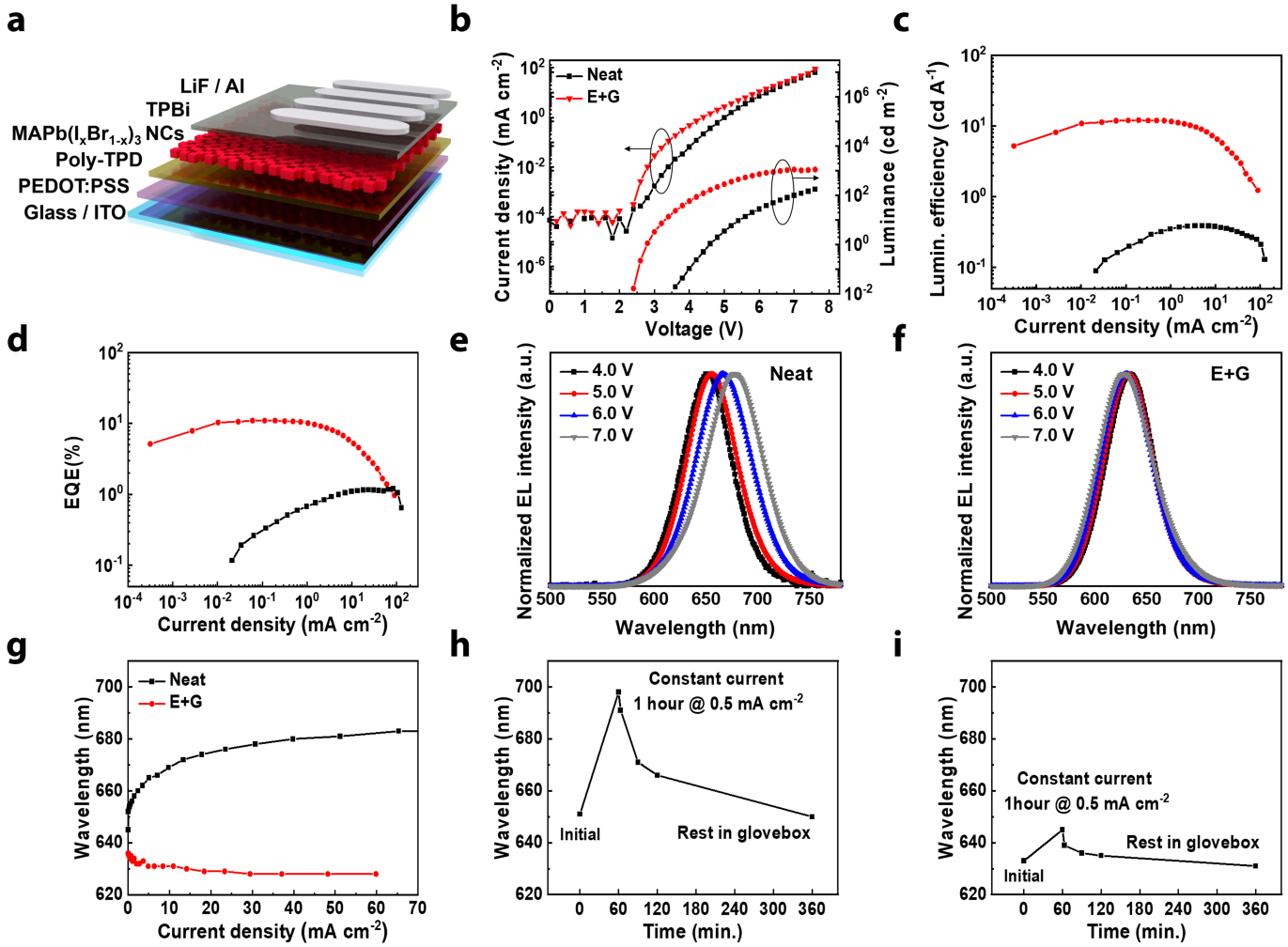

Extended Data Fig. 7 | Device characteristics and stability of the electroluminescence spectra of the mixed-halide MAPb(I_xBr_{1-x})$_3$ NC-LEDs. **a**, Schematic illustrations of the NC-LED configuration showing the device architecture: ITO/PEDOT:PSS/poly-TPD/MAPb($I_{1-x}Br_x$)$_3$ nanocrystals/TPBi/LiF/Al. **b**, Current density–voltage (*J*–*V*) and luminance–voltage (*L*–*V*) curves of NC-LEDs. **c**, Luminous efficiency plotted against current density for NC-LEDs. **d**, EQE–current density curves of NC-LEDs. **e**, **f**, Electroluminescence spectra of neat (**e**) and E+G-treated (**f**) NC-LEDs at different bias voltages. **g**, Peak wavelength of electroluminescence of neat and E+G-treated NC-LEDs at different current densities. **h**, **i**, Peak wavelength of electroluminescence of neat (**h**) and E+G-treated (**i**) NC-LEDs at a constant current of 0.5 mA cm^{-2} for one hour, followed by measurements of the same device after resting in the glove box for the indicated times. The electroluminescence peak shifts under the constant current density of 0.5 mA cm^{-2} but recovers to its initial position after resting in the glove box for 5 h, indicating the reversibility of halide segregation.

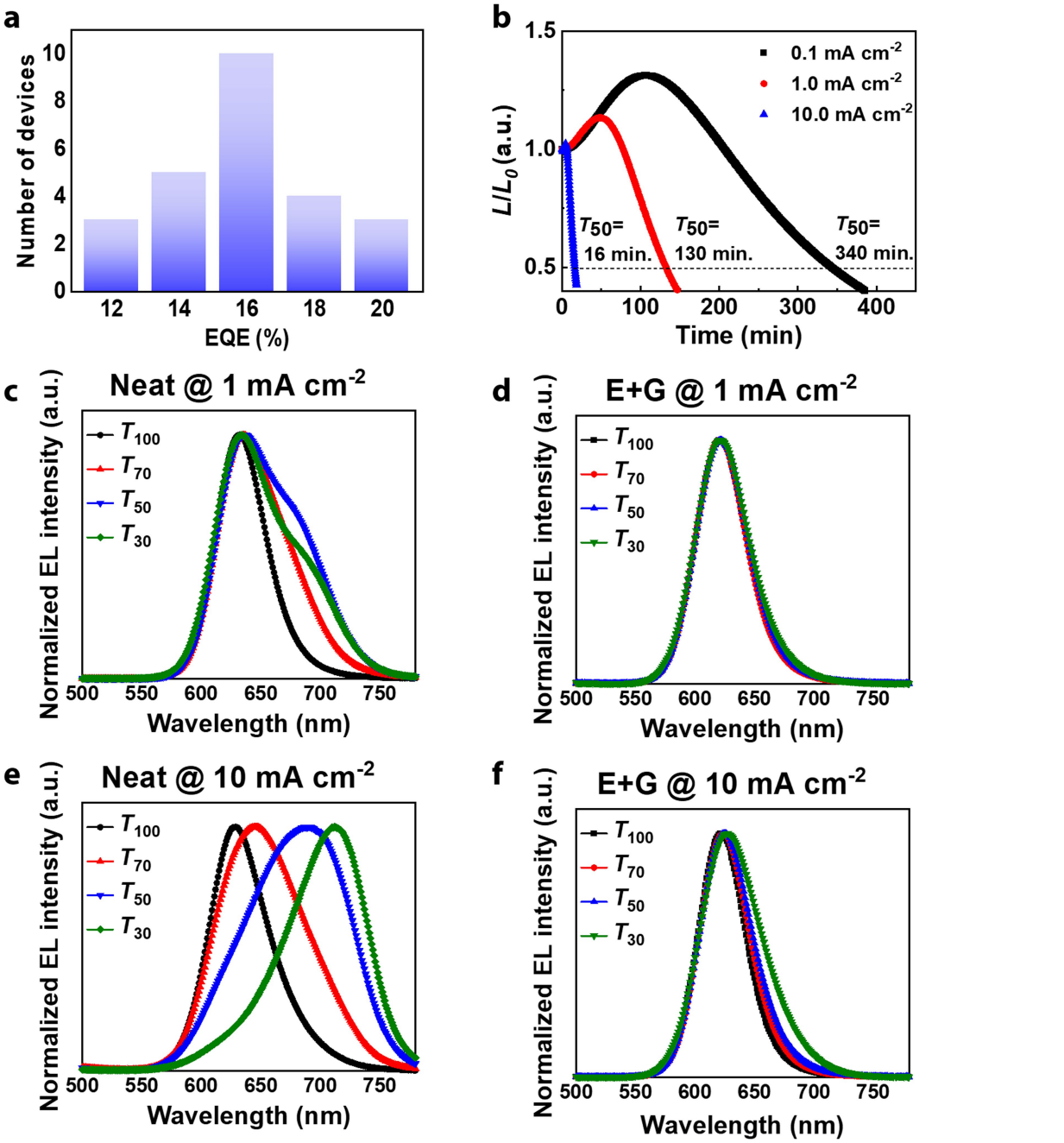

Extended Data Fig. 8 | Histogram of maximum EQE values and operating stability of mixed-halide MAPb(I_xBr_{1-x})$_3$ NC-LEDs. a, Histogram of maximum EQE values for E+G-treated NC-LEDs, collected from 25 devices. **b**, Operational stability of E+G-treated NC-LEDs measured in air at a constant current of 0.1 mA cm^{-2} (initial luminance (L_0) = 22 cd m^{-2}), 1 mA cm^{-2} (L_0 = 141 cd m^{-2}) and 10 mA cm^{-2} (L_0 = 585 cd m^{-2}). **c**–**f**, Electroluminescence spectra of NCs-LEDs with neat (**c**, **e**) and E+G ligand-treated (**d**, **f**) nanocrystal layers at a different lifetimes and with constant current densities of 1 mA cm^{-2} (**c**, **d**) and 10 mA cm^{-2} (**e**, **f**).

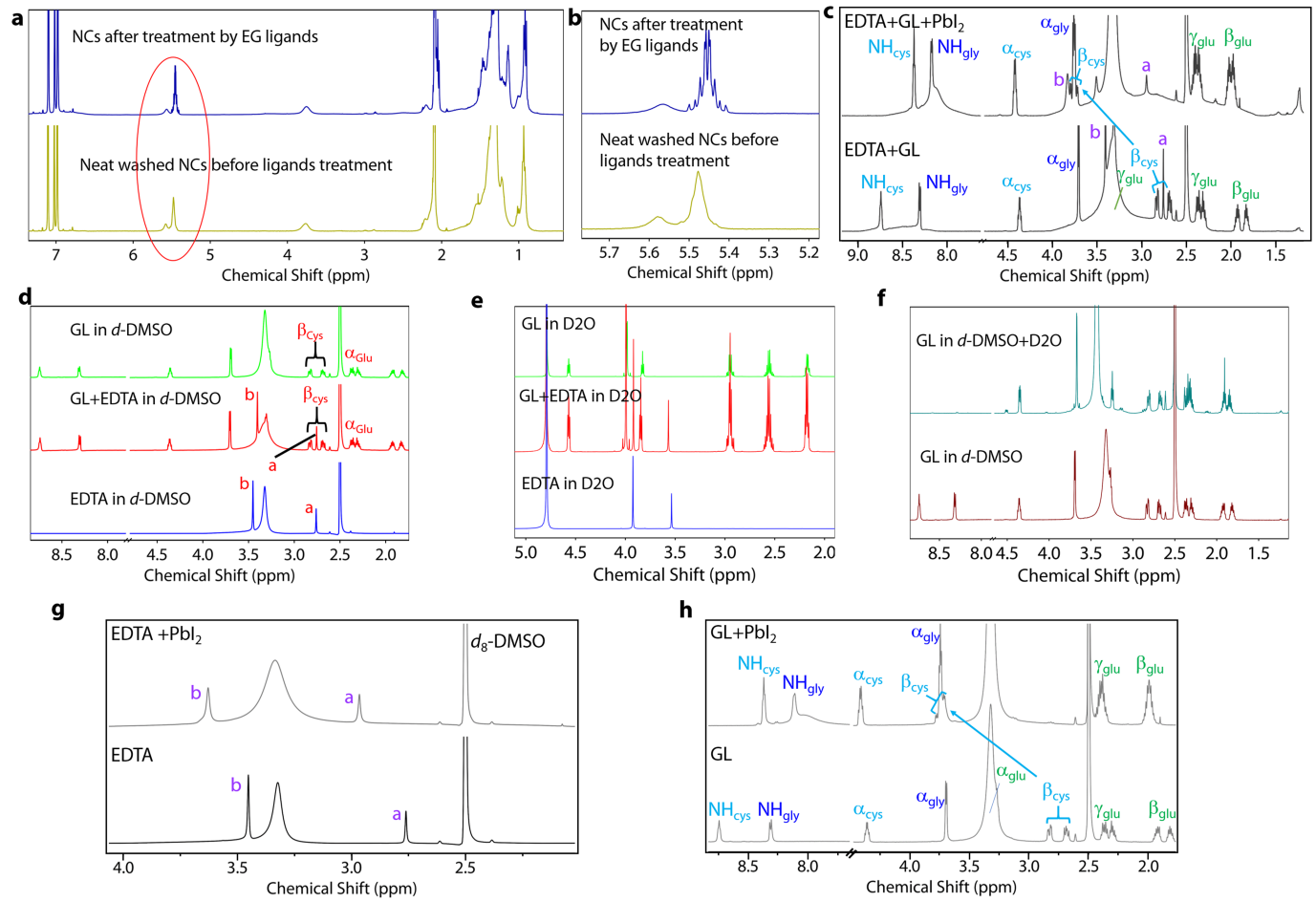

Extended Data Fig. 9 | ^{1}H NMR spectra of solutions. a, $MAPb(I_xBr_{1-x})_3$ nanocrystals before and after treatment with E+G mixture in d_8-toluene. **b**, Magnification of the circled region of the ^{1}H NMR spectra in **a** (between 5.4 and 5.6 ppm), showing details of the proton bound to C=C of oleic acid/oleylamine. Fine structure can be seen on top of the broad resonance after ligand treatment, which is indicative of free oleic acid and oleylamine ligands. **c**, Systematic addition of E+G to PbI_2 in d_6-DMSO solutions. **d**, **e**, EDTA, glutathione and E+G in d_6-DMSO (**d**) and D_2O (**e**). When both ligands are combined in the E+G mixture, the individual peak positions are retained, indicating that there is no chemical interaction between the two ligands. **f**, Glutathione in d_6-DMSO and in a mixture of d_6-DMSO with D_2O, showing the disappearance of the amide NH peaks (corresponding to exchangeable protons) in the presence of D_2O. **g**, **h**, Systematic addition of EDTA (**g**) and glutathione (**h**) to PbI_2 in d_6-DMSO solutions.

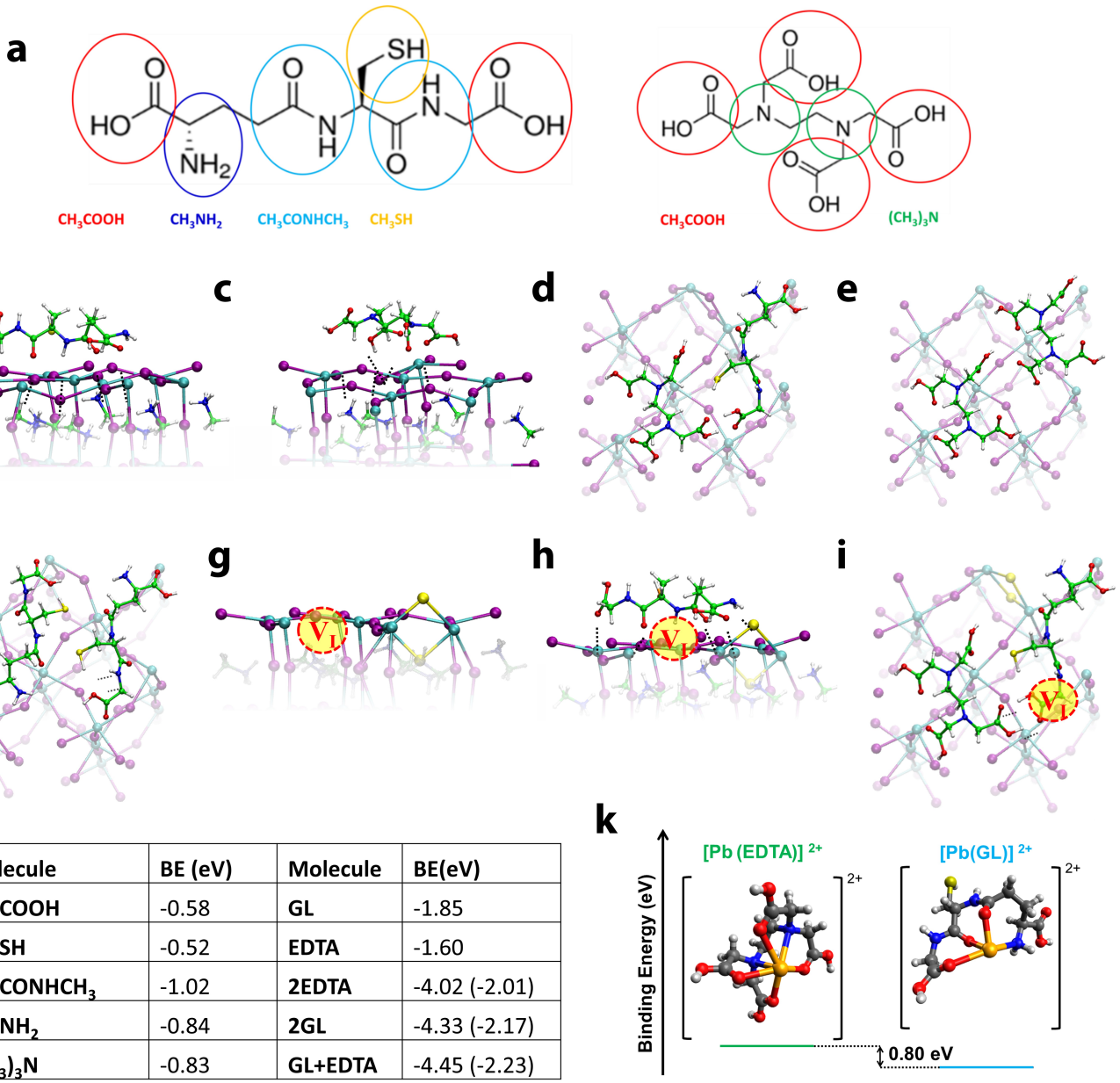

Molecule	BE (eV)	Molecule	BE(eV)
CH_3COOH	-0.58	GL	-1.85
CH_3SH	-0.52	EDTA	-1.60
$CH_3CONHCH_3$	-1.02	2EDTA	-4.02 (-2.01)
CH_3NH_2	-0.84	2GL	-4.33 (-2.17)
$(CH_3)_3N$	-0.83	GL+EDTA	-4.45 (-2.23)

Extended Data Fig. 10 | DFT-optimized structures of surface-adsorbed ligands. a, Structure of glutathione (left) and EDTA (right), with fragments that were used to study their interaction with the perovskite highlighted. **b**–**f**, DFT-optimized structures of surface-absorbed glutathione (**b**), EDTA (**c**) one glutathione molecule and one EDTA molecule (**d**), two EDTA molecules (**e**) and two glutathione molecules (**f**). **g**–**i**, The optimized structure of an iodine Frenkel defect pair (defective iodine atoms in yellow) on the bare PbI_2-terminated perovskite surface (**g**), in the presence of adsorbed glutathione (**h**) and in the presence of adsorbed E+G (**i**). The iodine vacancy is highlighted with a dashed circle. **j**, Binding energies of fragments and complete molecules to the PbI_2-terminated perovskite surface. Data in parenthesis is the value per adsorbed molecule. **k**, DFT-optimized structures of the Pb^{2+} complexes with EDTA and with glutathione. The relative binding energies showing that EDTA binds more strongly to Pb^{2+} than does glutathione by 0.80 eV.